Sublimation waves: Geomorphic markers of interactions between icy planetary surfaces and winds

M Bordiec, Sabrina Carpy, Olivier Bourgeois, C. Herny, M Massé, L. Perret, P. Claudin, S Pochat, Sylvain Douté

Sublimation waves: Geomorphic markers of interactions between icy planetary surfaces and winds

M. Bordiec, S. Carpy, O. Bourgeois, C. Herny, M. Massé, L. Perret, P. Claudin, S. Pochat, S. Douté

PII: S0012-8252(20)30396-2

DOI: https://doi.org/10.1016/j.earscirev.2020.103350

Reference: EARTH 103350

To appear in: *Earth-Science Reviews*

Received date: 7 January 2020

Revised date: 15 July 2020

Accepted date: 21 August 2020

Please cite this article as: M. Bordiec, S. Carpy, O. Bourgeois, et al., Sublimation waves: Geomorphic markers of interactions between icy planetary surfaces and winds, *Earth-Science Reviews* (2020), https://doi.org/10.1016/j.earscirev.2020.103350

Sublimation waves: geomorphic markers of interactions between icy planetary surfaces and winds

M. Bordiec[a], S. Carpy[a], O. Bourgeois[a], C. Herny[b], M. Massé[a], L. Perret[c], P. Claudin[d], S. Pochat[a], S. Douté[e]

[a] Laboratoire de Planétologie et Géodynamique, Université de Nantes, Université d'Angers, CNRS, UMR 6112, Nantes, France

[b] Physikalisches Institut, Universität Bern, Bern, Switzerland

[c] Laboratoire de recherche en Hydrodynamique, Énergétique et Environnement Atmosphérique, Centrale Nantes, CNRS, UMR 6598, Nantes, France

[d] Laboratoire de Physique et Mécanique des Milieux Hétérogènes, ESPCI, Université Paris-Diderot, Université Pierre et Marie Curie, CNRS, UMR 7636, Paris, France

[e] Université Grenoble Alpes, Institut de Planétologie et d'Astrophysique de Grenoble (IPAG), CNRS, UMR 5274, Grenoble, France

Abstract

Sublimation waves are periodic, linear and transverse bedforms that grow by sublimation of icy substrates under turbulent winds. They occur in different environments of the Earth and other planets, where the climate is favorable to sublimation. Their morphological and kinematic characteristics (wavelength, migration velocity, characteristic time of formation) depend on the environmental conditions in which they develop (atmosphere viscosity, wind speed, sublimation rate). To highlight these relations, we designed a theoretical model for their formation, based on models previously designed for dissolution bedforms. From a linear stability analysis of the model, we derived a dispersion relation and three scaling laws. These are validated by comparison with measurements available for two natural terrestrial examples (Blue Ice Areas of the Antarctic ice sheets and ice caves) and with new measurements in a laboratory experiment. They are applied to linear bedforms, of hitherto unknown origin, that we identified on the Martian North Polar Cap. We thus demonstrate that sublimation waves are convenient geomorphic markers to constrain surface compositions, atmospheric properties, climates, and winds on terrestrial ice sheets and other icy planetary surfaces.

Keywords:

sublimation, planetary surfaces, bedforms, instability, scaling laws, wind, ice sheets

Email address: mai.bordiec@univ-nantes.fr (M. Bordiec)

Nomenclature

Greek symbols

κ	Von Karman constant, $\kappa \approx 0.41$ [dimensionless]
λ	wavelength of the waves [m]
ν	kinematic viscosity of the fluid [$\mathrm{m^2 \cdot s^{-1}}$]
ω	angular frequency of the waves [$\mathrm{rad \cdot s^{-1}}$]
$\rho_{\bullet}$	density of $\bullet$ [$\mathrm{kg \cdot m^{-3}}$]
σ	growth rate of the waves [$\mathrm{s^{-1}}$]
τ_{xz}	shear stress of the flow [$\mathrm{kg \cdot m^{-1} \cdot s^{-2}}$]
θ_{q}	mass transfer phase lag [°]
ζ	height of the interface ice-flow [m]
ζ_0	half-amplitude of the waves [m]

Roman symbols

D	diffusion coefficient of ice vapour into the flow [$\mathrm{m^2 \cdot s^{-1}}$]
H	height of the boundary layer flow [m]
k	wavenumber of the waves [$\mathrm{m^{-1}}$]
Ls	solar longitude [°]
F	linear correction of the sublimation flux [dimensionless]
$M_{\bullet}$	molar mass of $\bullet$ [$\mathrm{kg \cdot mol^{-1}}$]
p	total pressure [Pa]
p_v	partial vapour pressure [Pa]
p_{sat}	saturated vapour pressure [Pa]
q	sublimation flux [$\mathrm{kg \cdot m^{-2} \cdot s^{-1}}$]
R_a	aspect ratio [dimensionless]
Re_H	global Reynolds number [dimensionless]
RH	relative humidity [%]
Sc	Schmidt number [dimensionless]

SH	specific humidity [%]
T	ambiant temperature [K]
t	time [s]
t_c	characteristic time of formation [s]
T_{sat}	temperature at saturation [K]
T_t	temperature at the triple point [K]
$\vec{u}$	flow speed [$\mathrm{m \cdot s^{-1}}$]
U	mean flow speed [$\mathrm{m \cdot s^{-1}}$]
u_*	friction velocity or shear velocity [$\mathrm{m \cdot s^{-1}}$]
$u_x(z)$	flow speed at height z in the x direction [$\mathrm{m \cdot s^{-1}}$]
v	migration velocity of sublimation waves [$\mathrm{m \cdot s^{-1}}$]
x	horizontal coordinate of the main flow direction [m]
z	vertical coordinate [m]

Superscripts and subscripts

$\bullet^+$	dimensionless form of $\bullet$
$\bullet^0$	base state of $\bullet$ (flat surface)
$\bullet_c$	critical $\bullet$ (most unstable mode)
$\bullet_f$	$\bullet$ of the fluid
$\bullet_s$	$\bullet$ of the ice surface
$\bullet_{int}$	$\bullet$ at the interface ice-flow

1. Introduction

Aeolian processes are central geomorphic agents on many bodies of the Solar System (Bourke et al., 2010; Craddock, 2012; Lorenz and Zimbelman, 2014; Cohen-Zada et al., 2016): they produce bedforms such as ripples, dunes, yardangs and streaks. These ”loose bedforms”, which derive from mechanical transport of loose granular materials (Figure 1a and 1c), have been observed and well documented, in particular on Earth (Cooke et al., 1993; Lancaster, 1995; Livingstone and Warren, 2019), Mars (Hayward et al., 2007; Fenton and Hayward, 2010), Titan (Lorenz and Radebaugh, 2009), Venus (Greeley et al., 1997), comet

67P/Churyumov-Gerasimenko (Thomas et al., 2015; Jia et al., 2017) and Pluto (Telfer et al., 2018). The geometric and kinematic characteristics of these bedforms (e.g., shape, size, orientation, migration direction, migration velocity and growth rate) can be determined by field measurements or remote sensing. Aeolian bedforms thus constitute convenient geomorphic markers to constrain surface/atmosphere interactions on the solid bodies of the Solar System. For example, they have been abundently used to constrain or validate atmospheric, climatic or wind numerical models on Earth (Blumberg and Greeley, 1996), Mars (Greeley et al., 1993; Lee and Thomas, 1995; Fenton and Richardson, 2001; Fenton et al., 2005; Lapotre et al., 2016, 2018; Durán et al., 2019), Titan (Tokano, 2008, 2010; Charnay et al., 2015; Rodriguez et al., 2018), Pluto (Telfer et al., 2018) and comet 67P/Churyumov-Gerasimenko (Jia et al., 2017). Conversely, from known atmospheric and surfaces conditions, scaling laws can be used to predict aeolian bedforms characteristics in other planetary environments (Claudin and Andreotti, 2006).

For these purposes, the physics behind the formation and development of aeolian bedforms has to be sufficiently well understood. This is relatively true for "loose bedforms" (Schmidt, 1980; Kok et al., 2012; Durán et al., 2011; Charru et al., 2013; Courrech du Pont, 2015). However, it is still not the case for "solid bedforms" that are produced by mass transfers between solid substrates such as ices or rocks and fluid flows. Phase transitions (sublimation and condensation, melting and freezing) and chemical reactions (dissolution and precipitation) are the main processes possibly involved in the generation of these "solid bedforms" (Thomas, 1979; Allen, 1982; Meakin and Jamtveit, 2010) (Figure 1b and 1d).

[[Image]]

Figure 1: Physical processes possibly involved in the formation of bedforms. (a) Example of "loose bedforms": image of a sand ripples field (Erg Chebbi, Morocco, credit: Thomas Hartmann). The wavelength of ripples is decimetric. (b) Example of "solid bedforms": image of a sublimation wave field (Blue Ice Area in Svea, Antarctica, (Bintanja et al., 2001)). The wavelength of sublimation waves is on the order of $20\,\mathrm{cm}$. (c) Matter transfers in "loose bedforms" are controlled by mechanical transport of particles, by either creeping, saltation or suspension. (d) Matter transfers in "solid bedforms" are controlled by chemical reactions or phase changes between a solid substrate and a flowing fluid. Illustrated is the case of sublimation: spatial variations in the sublimation rate lead to differential ablation of the substrate.

While sublimation plays only a minor role in shaping terrestrial landscapes, it is potentially

more effective on other planets (Mangold, 2011) such as Mars (Hofstadter and Murray, 1990; Skorov et al., 2001), on icy bodies (Consolmagno and Lewis, 1978) such as Pluto (Moore et al., 2018; White et al., 2017; Protopapa et al., 2017; Bertrand et al., 2018), Ceres (Nathues et al., 2015; Formisano et al., 2016), Callisto (Howard and Moore, 2008), Ganymede (Squyres, 1980), Iapetus (Kimura et al., 2011), but also on Io (Ingersoll et al., 1985) and on comets (Keller et al., 2015; Sunshine et al., 2016). We thus explore here the development of a specific class of solid bedforms, made by sublimation of an icy solid substrate and diffusion of the corresponding vapour in the flow of a different gas (Figure 1b).

These processes may lead to the development of either bowl-shaped depressions, known as scallops or cups (Curl, 1966; Bintanja et al., 2001), or periodic linear bedforms, displaying a regular spacing and an orientation transverse to the main wind direction (Curl, 1966; Weller, 1969; Bintanja et al., 2001). We focus on the latter, which we propose to name "sublimation waves".

First, we compile data currently available in the literature about their development conditions and morphological characteristics in two terrestrial settings: Blue Ice Areas of the Antarctic Ice Sheet and ice caves. Then, we provide new observationnal data on candidate sublimation waves on the North Polar Cap of Mars. We complement this natural observational dataset with the results of a new laboratory experiment performed in a wind tunnel.

Then, to explore the physics that govern the development of sublimation waves, we adapt the stability analysis of a theoretical model initially designed for dissolution bedforms by Claudin et al. (2017). Using the relevant parameters for sublimation waves, we derive a dispersion relation and three scaling laws for sublimation waves. These relate some morphological and kinematic characteristics (wavelength, migration velocity, characteristic time of formation) of sublimation waves to their environmental conditions (atmosphere viscosity, wind speed, sublimation rate). These laws are compared to observations in natural systems (Earth, Mars) and in our experiment for validation and for prediction of missing data in some of these systems. Based on these new scaling laws, sublimation waves can be employed as markers of surface/atmosphere interactions on ice sheets and icy planetary surfaces.

2. Sublimation waves in nature and experiments

2.1. Conditions required for sublimation

Sublimation is the direct phase transition from solid to gas without passing through a liquid phase. Sublimation of water ice can occur on the whole ranges of temperatures of the ice-vapour

interface T_{int} and partial water vapour pressures p_v, for which the solid and gaseous phases coexist (Figure 2a). It requires energy as it is an endothermic process. At any atmospheric pressure p, the sublimation flux q of ice depends on its temperature and the relative humidity RH of the atmosphere, which is the ratio of the partial pressure of water vapour to the saturated vapour pressure p_{sat} at a given temperature. Relative humidity is different from specific humidity SH, which is a measure of the moist content and is defined as the ratio of the mass of water vapour to the total mass of moist air in a parcel. Sublimation can occur as long as $RH < 100\%$ and $T_{int} < T_t$, where T_t is the temperature of the triple point. The lower the relative humidity is, the more sublimation is effective (Law and Van Dijk, 1994), as indicated by the typical Hertz-Knudsen law: $q \propto p_v - p_{sat}$.

[[Image]]

Figure 2: Phase diagrams (p, T) for (a) H_2O and (b) CO_2. The saturated water vapour pressure p_{sat} (black lines) is the pressure at which the solid and the gaseous phases are at equilibrium, at a given temperature. The saturated vapour pressure follows the Clausius-Clapeyron relation. For sublimation to occur, the partial vapour pressure p_v in the atmosphere must be such that $p_v < p_{sat}(T)$ for temperatures below the triple point ($T < 273\,\mathrm{K}$ for water and $T < 216\,\mathrm{K}$ for CO_2). For partial water vapour pressures below the triple point ($p_v < 611\,\mathrm{Pa}$ for water and $p_v < 5.18\times10^5\,\mathrm{Pa}$ for CO_2), sublimation occurs when temperatures are such that $T > T_{sat}(p_v)$. Partial vapour pressures p_v at the temperature of the ice-vapour interface T_{int} and atmospheric total pressures p and temperature T are displayed for the different environments described in Sections 2.2, 2.3 and 2.4 (Blue Ice Areas, ice caves, Martian North Polar Cap and experimental model) and summarized in Table 1.

2.2. Observations on Earth

On Earth, the pressure, humidity and temperature conditions required for glacial surface sublimation are encountered in very specific settings only. This explains why terrestrial sublimation waves are rare and still poorly known. However, these conditions exist on some tropical glaciers of high altitude during the dry season (Winkler et al., 2009), in the Blue Ice Areas (BIAs) of Antarctica (van den Broeke and Bintanja, 1995) and in some ice caves (Obleitner and

Spötl, 2011). Sublimation waves have been observed in the latter two environments. From the literature, we compile here observations and measurements made on sublimation waves in these environments and complement some missing data by recomputing them (Table 1).

2.2.1. Blue Ice Areas (BIAs)

BIAs are regions at the surface of ice sheets, where ablation is so efficient, that previously buried layers of old and blue ice are exhumed. They have been described in Antarctica only, where they cover approximately 1% of the continent (Giovinotto, 1964) (Figure 3a). BIAs usually display specific environmental and meteorological conditions (Table 1), such as typical atmospheric pressures between 800 hPa and 850 hPa (Bintanja, 1999). The atmosphere over BIAs is dry, as the specific humidity varies between 0.085% and 0.12% in the first 100 m above the surface (van den Broeke and Bintanja, 1995), leading to partial vapour pressures between 110 Pa and 160 Pa and relative humidities between 30% and 50%. Atmospheric temperatures above the surface (2 m) vary between -14°C and -7°C during the austral summer and the temperature of the ice-air interface is almost equal to the atmospheric temperature (Bintanja, 1999). The low albedo of ice (0.6) compared to that of snow (0.8) increases the absorption of solar radiations, and so the energy available for sublimation in BIAs.

[[Image]]

Figure 3: BIAs in Antarctica. (a) Map of the Antarctic continent with superimposed locations of ice shelves and BIAs (Winther et al., 2001; Fretwell et al., 2013; Hui et al., 2014). (b) Location of the BIA studied by Bintanja et al. (2001) and Bintanja R. (1995) in Svea, Scharffenbergbotnen valley, Queen Maud Land. 74°35′0″ S, 11°13′0″ W. Dominant winds flow from east to west. Image is from Google Earth V 7.3.2.5495. (December 1, 2011). Eye alt 21.83 km. DigitalGlobe 2018. http://earth.google.com.

The surface temperature on BIAs is such that $T < 273$ K and the partial water vapour pressure is such that $p_v < p_{sat}$ throughout the year (Figure 2a). In these areas, ablation is thus mainly induced by sublimation. The annual surface mass balance of BIAs is negative, with higher sublimation rates (lower RH that induces lower p_v) in summer than in winter. Sublimation rates of approximately $10\,\mathrm{cm \cdot yr^{-1}}$ were measured for steady states during the austral summer (Bintanja et al., 2001), and were validated by comparison to latent heat fluxes deduced from

surface energy balance (Bintanja R., 1995).

The slightest snow accumulation on BIAs is blown away by katabatic winds that flow on their aerodynamically smooth surfaces (Bintanja, 1999). Mean wind speeds are generally higher on BIAs (between $2\,\mathrm{m}\cdot\mathrm{s}^{-1}$ and $8\,\mathrm{m}\cdot\mathrm{s}^{-1}$ at $6\,\mathrm{m}$ above the surface) than on the surrounding snow surfaces (van den Broeke and Bintanja, 1995). Those winds are turbulent, as indicated by the short-time variability in recorded atmospheric pressures (Bintanja, 1999).

Parameters: symbols [units]	BIA (Svea in summer)	Ice cave (Eisriesenwelt in winter)	MNPC (summer)	Exp.
	(H_2O ice - air)	(H_2O ice - air)	(H_2O ice - atm.)	(CO_2 ice - CO_2 air)
Molar mass (ice): M_s $[kg\cdot mol^{-1}]$	0.018	0.018	0.018	0.044
Molar mass (fluid): M_f $[kg\cdot mol^{-1}]$	0.029	0.029	0.044	0.029
Density (ice): $\rho_s[kg\cdot m^{-3}]$	$850-880$ [1,2,3]	870 ± 18 [4]	917 (a)	1562
Ice-fluid interface temperature: $T_{int}[K]$	266 [5]	272 [6,7]	220 [8]	198
Ambiant temperature: $T[K]$	265 [5]	272 [6,7]	210 [8]	293
Atmospheric pressure: $p[Pa]$	80000 – 85000 [5]	101300 [6]	$715-740$ [9,10]	101300
Specific humidity: $SH[\%]$	$0.085-0.12$ [3]	0.3 (b)	0.06 (b)	0.05 (b)
Relative humidity: $RH[\%]$	$30-50$ (c)	97.5 [7]	$23-27$ (c)	20 (c)
Partial vapour pressure:	$110-166$ (b)	516 (c)	$0.6-0.7$ (d)	40 (e)

$p_v[Pa]$				
Saturated vapour pressure: $p_{sat}(T)[Pa]$	336 (f)	530 [7]	2.6 (f)	1.4×10^5
Temperature at saturation: $T_{sat}(p_v)[K]$	$254-258$ (f)	271 (f)	$209-210$ (f)	128 (f)

Table 1: Average environmental conditions in the BIA in Svea during austral summer, the Eisriesenwelt ice cave in winter, the Martian North Polar Cap (MNPC) at 80°N for $110^\circ < Ls < 120^\circ$, and the experimental model. [1] Weller (1969). [2] Mellor and Swithinbank (1989). [3] van den Broeke and Bintanja (1995). [4] May et al. (2011). [5] Bintanja (1999). [6] Curl (1966). [7] Obleitner and Spötl (2011). [8] Pankine et al. (2010). [9] Forget et al. (1999). [10] Millour et al. (2018). (a) The standard density of water ice is considered here, as the dust content estimated on the entire MNPC (Barr and Milkovich, 2008) is sufficiently small ($< 2\%$ by mass) that it can be neglected. (b) The relation $SH = \frac{p_v M_s / M_f}{p - (1 - M_s / M_f) p_v}$ is used either to compute the specific humidity or the partial vapour pressure, depending on the available data. (c) The definition $RH = \frac{p_v}{p_{sat}}$ of the relative humidity is used. (d) The partial water vapour pressure on the MNPC is deduced from water vapour column abundances (Pankine et al., 2010). (e) The partial CO_2 vapour pressure in the experiment conditions is derived from the standard volume fraction of CO_2 in air. (f) The saturated vapour pressure and the temperature at saturation were computed with the Clausius-Clapeyron relation.

The surface of some BIAs displays typical examples of sublimation waves (Mellor and Swithinbank, 1989). These have been described in details in the Svea station ($74^\circ35'0''$ S, $11^\circ13'0''$ W), Queen Maud Land (Bintanja et al., 2001; van den Broeke and Bintanja, 1995; Bintanja, 1999; Bintanja R., 1995) (Figure 3b). They are regularly spaced and parallel crested ridges, transverse to the strongest winds (Bintanja et al., 2001; Mellor and Swithinbank, 1989) (Figure 4a and 4b). In map-view, they display bifurcations and junctions, similar to those observed on aeolian sandy ripples and dunes (Cooke et al., 1993; Lancaster, 1995; Livingstone and Warren, 2019). In cross-section, they can be either symmetrical (Figure 4c) or asymmetrical, with a

steepest slope on the lee side (Bintanja et al., 2001).

[[Image]]

Figure 4: Typical morphology of sublimation waves in a BIA. (a) Image of the regularly rippled surface of the BIA in Svea (Bintanja, 1999). Black lines highlight some of the crests while white arrows show the orientation of the main wind direction. (b) Typical cross-sectional profile (Bintanja et al., 2001).

Their typical wavelengths and heights cover wide ranges of values, from $5\,\mathrm{cm}$ to $25\,\mathrm{cm}$, and from $1\,\mathrm{cm}$ to $10\,\mathrm{cm}$, respectively (Weller, 1969; Bintanja et al., 2001; Mellor and Swithinbank, 1989). Their aspect ratio (i.e. wavelength/height), is less than 0.1 in Svea but can reach up to 0.5 in other places (Mellor and Swithinbank, 1989). Both their shapes and heigths can vary over time. They migrate in the downwind direction with a maximal measured velocity of $2\,\mathrm{cm}\cdot\mathrm{month}^{-1}$ (Bintanja et al., 2001).

2.2.2. Ice caves

[[Image]]

Figure 5: Typical morphology of sublimation waves in Eisriesenwelt (Salzburg, Austria). The wavelength is on the order of $140\,\mathrm{cm}$ (Curl, 1966). The white arrow shows the direction of air flow on the icy wall and the black lines highlight the crests.

Ice caves are found in all regions of the Earth outside the tropics and are defined as rock caves, which contain seasonal or perennial ice (Ford and Williams, 1989). Conceptual models of ice cave climates have been built from long-term meteorological measurements (Peroiu et al., 2011), especially in the Eisriesenwelt cave (Salzburg, Austria) (Obleitner and Spötl, 2011). As in many ice caves, the ice surface temperature in Eisriesenwelt is about $-1.5^{\circ}C$ during winter and reaches $0^{\circ}C$ in summer. The relative humidity RH is high ($RH = 97.5\%$) in average throughout the year but the air is dry, especially in winter ($SH = 0.3\%$, computed from the existing measurements), with partial water vapour pressures around $520\,\mathrm{Pa}$ (Figure 2a, Table 1). Sublimation thus occurs dominantly in winter when dry, cold and turbulent air circulates at speeds up to $0.2\,\mathrm{m}\cdot\mathrm{s}^{-1}$ (Curl, 1966; Obleitner and Spötl, 2011; Bella, 2007). Sublimation rates during winter have not been measured directly in the Eisriesenwelt cave but have been estimated in other ice caves. The annual ablation rate due to sublimation in ice caves can be as low as $3\,\mathrm{mm}\cdot\mathrm{yr}^{-1}$ (Marshall and Brown, 1974) and as high as $35\,\mathrm{mm}\cdot\mathrm{yr}^{-1}$ (Persoiu and Lauritzen, 2018), leading to

sublimation rates between $3.8\times10^{-10}\,\mathrm{m\cdot s^{-1}}$ and $4.5\times10^{-9}\,\mathrm{m\cdot s^{-1}}$, if the ablation is restricted to winter, when sublimation is most effective.

The walls of many ice caves display bedforms induced by sublimation (Curl, 1966; Bella, 2007; Cigna and Forti, 2012). Among them, sublimation waves are regular, periodic, parallel crested patterns, transverse to the air flow direction (Curl, 1966). Their lee slope is steeper than their stoss slope. Their average wavelength is on the order of $140\,\mathrm{cm}$ and their height is between $0.1\,\mathrm{m}$ and $0.3\,\mathrm{m}$, leading to an aspect ratio between 0.07 and 0.2. Their migration in the downflow direction has been mentioned but not measured (Curl, 1966).

2.3. Martian North Polar Cap

The Martian North Polar Cap (MNPC) is composed of ice mixed with minor amounts of dust. The major processes involved in its present-day evolution are condensation and sublimation of H_2O and CO_2 ices (Hofstadter and Murray, 1990; Skorov et al., 2001). CO_2 vapour constitutes up to 95% of the Martian atmosphere and this amount is seasonally variable (Kieffer et al., 1976): CO_2 vapour condenses and precipitates as frost on the MNPC in winter and sublimates in spring and summer. The CO_2 seasonal cap is thus ephemeral (James, 1982; Kelly et al., 2007). While sublimating, the CO_2 cap reveals gradually the underlying perennial water ice cap, which is exposed to sublimation in turn (Kieffer et al., 1976). Water ice sublimation occurs in early summer ($90^\circ < Ls < 120^\circ$) with a maximum between $Ls = 110^\circ$ and $Ls = 120^\circ$. A water recondensation period occurs in late summer ($135^\circ < Ls < 164^\circ$) (Pankine et al., 2010; Brown et al., 2016).

The atmospheric pressure on the MNPC for latitudes between $80^\circ N$ and $90^\circ N$ varies from $600\,\mathrm{Pa}$ to $900\,\mathrm{Pa}$ during summer (Forget et al., 1999; Millour et al., 2018). At these latitudes, the average surface temperature varies from $150\,\mathrm{K}$ to $220\,\mathrm{K}$ throughout the year, and is highest ($220\,\mathrm{K}$) between $Ls = 110^\circ$ and $Ls = 120^\circ$ (Pankine et al., 2010). During this period, the atmosphere is very dry ($SH < 0.1\%$) even if the relative humidity is high ($RH \approx 25\%$). The partial water vapour pressures deduced from water vapour column abundances (between $55\,\mathrm{pr}-\mu\mathrm{m}$ and $65\,\mathrm{pr}-\mu\mathrm{m}$) given by TES data (Pankine et al., 2010) and CRISM data (Khayat et al., 2019) are thus very low (between $0.6\,\mathrm{Pa}$ and $0.7\,\mathrm{Pa}$, Figure 2a, Table 1).

Sublimation rates on the Martian surface have been derived theoretically (Ingersoll, 1970;

Ivanov and Muhleman, 2000; Hecht, 2002; Dundas and Byrne, 2010) and experimentally (Chittenden et al., 2008) for various conditions of temperature and wind speed. As the sublimation rate appears to be only temperature-dependent for high relative humidities ($RH \approx 30\%$), we compute the sublimation rate for temperatures between $150\ \mathrm{K}$ and $220\ \mathrm{K}$ and find that it should vary respectively from $2\times10^{-15}\ \mathrm{m\cdot s^{-1}}$ to $2\times10^{-10}\ \mathrm{m\cdot s^{-1}}$ (Chittenden et al., 2008).

Turbulent katabatic winds flow in spring and summer over the entire MNPC (Howard, 2000; Kauhanen et al., 2008; Petrosyan et al., 2011). Wind speeds computed from general and mesoscale atmospheric circulation models $20\ \mathrm{m}$ above the surface are estimated between $2\ \mathrm{m\cdot s^{-1}}$ and $10\ \mathrm{m\cdot s^{-1}}$ between $Ls = 110^\circ$ and $Ls = 130^\circ$ (Smith and Spiga, 2018).

[[Image]]

Figure 6: The Martian North Polar Cap. (a) Image of the MNPC on October 16, 2006 taken by the Mars Orbiter Camera (MARCI) onboard the Mars Reconnaissance Orbiter (MRO) (image ID: PIA01928; credit: NASA/JPL/MSSS). The perennial water-ice cap (white) is visible, as well as the dark circumpolar sediments. (b) Location of the studied area ($84^\circ N$, $120^\circ E$). The dominant wind direction (white arrow) was interpolated from numerical simulations (Smith and Spiga, 2018) and morphological features (Massé et al., 2012).

Landforms observed at the Martian North Polar Cap surface include spiral troughs (Massé et al., 2012; Murray et al., 1972; Howard et al., 1982; Smith et al., 2013; Smith and Holt, 2015), undulations (Howard, 2000; Cutts et al., 1979; Herny et al., 2014), polar chasmae (Fisher, 1993; Warner and Farmer, 2008; Holt et al., 2010), arcuate scarps, dune fields (Howard et al., 1982; Edgett et al., 2003), scallops and pits (Malin and Edgett, 2001) and many small-scale features (Nguyen et al., 2020). Aeolian redistribution of surface material (ice, dust), deposition/condensation of ices and dust from the atmosphere (James, 1982; Jakosky, 1985; Kahn et al., 1992; Fanale et al., 1992) and ablation/sublimation due to solar radiations (Ivanov and Muhleman, 2000; Massé et al., 2012; Herny et al., 2014; Ng and Zuber, 2006; Smith and Holt, 2010) are assumed to be the major processes involved in the generation of these landforms (Howard, 2000).

To investigate the existence of possible sublimation waves on the MNPC, we used orbital images in the regions above $80^\circ\ \mathrm{N}$ in latitude, where water ice is exposed to sublimation between $Ls = 110^\circ$ and $Ls = 135^\circ$. On these images, we identified linear ridges at the limit between

Boreales Scopuli and Olympia Cavi ($82^{\circ}N, 120^{\circ}E$, Figure 6). No explanation has been proposed yet for the formation of these ridges but Nguyen et al. (2020) suggested that they are different from the classical aeolian Martian dunes and that another process is responsible for their formation. The orientation of the dominant winds there, as derived from mesoscale simulations (Smith and Spiga, 2018) and confirmed by frost streaks (Figure 7), is E-W. This area shows regular, linear and parallel ridges oriented N-S. These ridges are thus transverse to the dominant winds (Figure 7a). The ridges display bifurcations and junctions (Figure 7b).

To constrain the morphology of these ridges, we derived a digital elevation model (DEM) from stereoscopic HiRISE images with a horizontal spatial sampling of $25\,\text{cm/pixel}$. The DEM was computed with a combination of photogrammetric and photoclinometric techniques (Jiang et al., 2017; Douté and Jiang, 2019). The spatial resolution and relative vertical accuracy of the DEM are on the order of $25\,\text{cm/pixel}$ and $15-20\,\text{cm}$ respectively. Topographic profiles derived from the DEM show that the average wavelength of the ridges is $7 \pm 0.3\,\text{m}$, and their height is on the order of $0.3\,\text{m}$ to $0.5\,\text{m}$, although these values are close to the vertical accuracy of the DEM. The aspect ratio of the ridges is thus 0.08 at most, and their lee side is apparently steeper than their stoss side (Figure 7c). From a comparison of all HiRISE images available for this region, we could not observe a temporal evolution of the ridges between 2006 and 2019.

[[Image]]

Figure 7: Typical morphology of proposed sublimation waves on the MNPC. (a) Image of the regularly rippled surface (HiRISE image ID: PSP_009689; credit: NASA/JPL/University of Arizona) captured on August 20, 2008 during northern Martian summer ($Ls = 115^{\circ}$). The spatial resolution is $25\,\text{cm/pixel}$. The size of the largest images available in this area ($\approx 24\,\text{km}^2$) gives a lower bound of the overall surface covered by the linear ridges as they are visible on the entire images. The wind direction derived from numerical simulations (Smith and Spiga, 2018) and morphological features (Massé et al., 2012) is indicated (white arrow) as well as the orientation of wind streaks visible on the image (orange arrows). (b) Zoom on some sublimation waves: these are regular and parallel crested. Black lines highlight the troughs. The location of the topographic profile displayed in (c) is indicated (blue line). (c) Topographic profile derived from the high-resolution DEM computed from HiRISE images.

These linear ridges are made of water ice, as they can be observed only during summer,

when the CO_2 ice has completely disappeared. At this period, sublimation combined with katabatic winds occurs at this location. Their morphological characteristics are similar to those of sublimation waves in the Blue Ice Areas of Antarctica. Therefore we suggest they are Martian examples of sublimation waves.

2.4. Laboratory experiments

[[Image]]

Figure 8: Sketch of the experimental device. (a) The ambiant air is aspirated in the wind tunnel, generating a turbulent flow. (b) The turbulent wind flows from left to right above the carbone dioxide ice sample (grey box). The ramp is inclined (10°) and a 1 cm high step on its peak initiates a perturbation of the flow downwind on the planar surface. The ice plateform is 1 m long.

Apart from Blue Ice Areas in Antarctica (Section 2.2.1) and ice caves (Section 2.2.2), natural sublimation waves are rare on Earth. We also identified candidate sublimation waves on Mars (Section 2.3). To complement this sparse observational dataset and provide additionnal constraints on the development conditions of sublimation waves, we conducted physical experiments with CO_2 ice in an atmospheric wind tunnel. In air at 1013 hPa, the partial vapour pressure of CO_2 is 40 Pa and CO_2 ice sublimates as long as $T > T_{sat}(p_v) = -145^\circ\mathrm{C}$ (Figure 2b).

The experiment was performed at the Laboratoire de recherche en Hydrodynamique, Énergétique et Environnement Atmosphérique (LHEEA) in Nantes (France). The wind tunnel was 24 m long and 2 m × 2 m in section. A turbine aspirated the ambiant air ($T = 20^\circ C$, $p = 1$ bar), causing a wind speed of $U = 6\,\mathrm{m\cdot s^{-1}}$ through the test section. Turbulence was ensured with spires and fences located at the tunnel entry. A planar sample of CO_2 ice ($T_{int} = -75^\circ C$), of horizontal dimensions 1 m × 30 cm, was placed on the tunnel floor, in the centre of the test section (Figure 8a). The tunnel configuration imposed a thickness of the hydrodynamical boundary layer of 1 m. To perturb the flow, a ramp (slope=10°) and a step (1 cm) were fashioned in the sample, upwind the observation area. This shape caused separation of the turbulent boundary layer and flow re-attachment on the planar sample surface (Figure 8b). The environmental conditions of the experiment are given in Table 1. The measured sublimation rate without wind was $1.4\times10^{-6}\,\mathrm{m\cdot s^{-1}}$

.

[[Image]]

Figure 9: Experimental sublimation waves observed after 4 h on the surface of the carbon dioxide ice sample. Their wavelength is approximately 6.5 cm and their amplitude is less than 1 cm . The white arrow shows the direction of the wind and the black lines highlight the crests.

After 4 h , topographic waves were observed on the CO_2 ice sample (Figure 9). They were linear, perpendicular to the wind direction, displayed a spacing of about 6.5 cm and their heights were less than 1 cm . Due to technical constraints, we could not monitor their potential migration during the experiment. This experiment confirms that periodic aeolian bedforms can grow without grain transport, by sublimation of ice under turbulent winds. It complements the current database of observations in BIAs, in ice caves and on Mars with a new set of measurements, in different conditions.

3. Sublimation waves in theory

The natural and experimental examples described in Section 2 provide evidence that wind flow may lead to the development of sublimation waves on icy substrates. They also provide four different sets of quantitative data, corresponding to four different physical environments, against which theoretical models may be tested.

One theoretical model has been proposed for the development of sublimation waves (Bintanja et al., 2001). This model assumes that sublimation waves form in response to an instability of the coupled ice-wind system. Based on a linear stability analysis of this model, Bintanja et al. (2001) derived typical growth rates, migration rates and wavelengths for sublimation waves in BIAs (Section 2.2.1). Their results are in reasonable agreement with observations made on natural sublimation waves in terms of wavelengths but not in terms of migration direction: this model predicts a displacement of the waves in the upwind direction, which is contrary to observations. No other theoretical studies were dedicated specifically to the development of bedforms by sublimation.

Thomas (1979) and Allen (1982) however highlighted the morphological and physical similarities between various kinds of solid bedforms that result from different processes: sublimation/condensation of ice in flowing air, melting/freezing of ice in flowing water, and dissolution/precipitation of soluble rocks in flowing water. All these processes, which involve

ablation of (or accumulation on) a solid substrate and diffusion of the ablated (or accumulating) matter in a flowing fluid, are able to produce topographic patterns from flat surfaces (Meakin and Jamtveit, 2010). Based on measurements in natural occurences and in physical experiments, several authors performed dimensional analyses and/or derived scaling laws for the development of such bedforms by dissolution/precipitation (Curl, 1966; Goodchild and Ford, 1972; Blumberg and Curl, 1974; Short et al., 2005) and by melting/freezing (Ashton and Kennedy, 1972; Ashton, 1972). Others performed stability analyses of theoretical models designed for dissolution/precipitation bedforms (Thorness and Hanratty, 1979; Chan and Goldenfeld, 2007; Camporeale and Ridolfi, 2012a; Claudin et al., 2017) and for melting/freezing bedforms (Gilpin et al., 1980; Ueno, 2007; Ueno et al., 2010; Camporeale and Ridolfi, 2012b). Among these analyses, Hanratty (1981) demonstrated that a specific formulation of the relaxation of the pressure gradient in the fluid is required to model properly the feedback between the flow and the topography in these problems. This relaxation of the pressure gradient is not taken into account in the model by Bintanja et al. (2001). Therefore, we adapt here to the specific case of sublimation/condensation bedforms, the model and stability analysis initially proposed for dissolution/precipitation bedforms by Claudin et al. (2017), following the pioneering work of Hanratty (1981). A correspondence table between the notation system used by Claudin et al. (2017) and our own system is provided in Appendix A, since these problems may be modeled with similar formulations. They differ, however, in several important properties of the implied materials: fluid viscosity and velocity, momentum and mass diffusivities in the fluid, kinetics of the mass transfer at the interface, bed roughness. We take these differences into account here.

First, we describe the adapted model and the characteristic dimensionless numbers that are relevant for sublimation/condensation. Then we briefly review the aims and the methods of the stability analysis described in details by Claudin et al. (2017), and give the results of its adaptation to the sublimation/condensation problem. From these results, we eventually derive new scaling laws for the specific case of sublimation waves.

3.1. Description of the model

[[Image]]

Figure 10: (a) General configuration of the problem with the main parameters. (b) The diffusive flux q above the wavy surface is shifted by the phase lag θ_q, imposing the maximum q_{max} somewhere in the trough when the waves are unstable.

The formation of sublimation waves results from interactions between an icy substrate and the flow of an overlying turbulent boundary layer (Curl, 1966; Bintanja, 1999), where a phase transition (sublimation) controls matter transfers between the solid substrate and the flowing gas.

Natural sublimation waves are generally perpendicular to the main wind direction, thus the problem can be reduced to a two-dimensional plane where the x-axis is the horizontal migration direction and the z-axis is the vertical direction. To model the processes, we consider the flow of an atmospheric boundary layer of height H, kinematic viscosity ν and density ρ_f over an icy substrate of density ρ_s (Figure 10a). We consider that the interface between the substrate and the atmosphere is wavy, with a sinusoidal profile of height ζ, wavelength λ (or wavenumber k) and amplitude $2\zeta_0$. The interface is assumed to be hydrodynamically smooth and the flow turbulent. It is characterized by its friction velocity u_* on the substrate. This velocity is also called "shear velocity" as it is related to the shear stress $\tau_{xz_{int}}$ of the flow on the interface and to the fluid density ρ_f, by $\tau_{xz_{int}} = \rho_f u_*^2$. The friction velocity is extrapolated from a classical law of the wall on smooth and flat surfaces such as $u_x(z) = \frac{u_*}{\kappa} \ln\left(\frac{9zu_*}{\nu}\right)$, where $\kappa \approx 0.41$ is the Von Kármán constant, and $u_x(z)$ is the wind speed at height z in the x-direction perpendicular to the waves.

The mass transfer diffuses the sublimating ice vapour into an other gaseous species that composes the flow, with a diffusion coefficient D. We assume that the convective mass transfer (diffusive matter flux q, Figure 10b) at the interface may vary along the profile and may have a maximum q_{max} somewhere along the profile, shifted from the crests by a phase lag θ_q. The flux phase lag θ_q can vary from 0° to 360° from a crest to an other, with $\theta_q = 180^\circ$ meaning that the flux maximum is right in the middle of the troughs. This effect allows the growth of a range of wavelengths and their migration, depending on the location of this maximum. When the maximum is located in the troughs ($90^\circ < \theta_q < 270^\circ$), the waves grow in height and the corresponding wavelengths are called "unstable". When the maximum is located on the crests ($0^\circ < \theta_q < 90^\circ$ and $270^\circ < \theta_q < 360^\circ$), the waves reduce in height or disappear ($\theta_q \to 0^\circ$ or $\theta_q \to 360^\circ$) and the corresponding wavelengths are "stable". The crests migrate in the upwind direction, downwind direction or remain stationnary, according to whether the maximum is located on the downwind

side ($0^\circ < \theta_q < 180^\circ$), upwind side ($180^\circ < \theta_q < 360^\circ$), or right in the troughs, respectively (Figure 10b).

The hydrodynamic boundary layer is the layer of fluid flowing on a surface where the viscosity effects are significant. The flow velocity varies from zero at the surface to a maximal speed far from the surface. The thickness of the hydrodynamic boundary layer is defined as the region where the velocity is less than 99% of the far field velocity. As for the hydrodynamic boundary layer, the mass transfer and thus the concentration difference between the substrate and the fluid induces a concentration boundary layer. We define this concentration boundary layer as the region where the difference from the surface concentration is 99% of the difference in concentration between the free stream flow and the surface.

The equations of the model are the usual Navier-Stokes equations for the dynamics of the flow and the convection-diffusion equation for the mass transfer. The global turbulence of the boundary layer is taken into account by introducing fluctuating turbulent perturbations in the previous equations following the statistical turbulence modeling (RANS method), in which the closure problem is solved with a classical eddy viscosity model (Chassaing, 2000), with consideration to a specific treatment on the mixing length involving a relaxation on the pressure gradient (Loyd et al., 1970; Hanratty, 1981).

3.2. Characteristic dimensionless numbers of the model

Five characteristic dimensionless numbers are relevant for the model. We review these numbers and discuss the significance of their values in the different environments described in Section 2. The values of the parameters displayed on Figure 10 are given for the different environments in Table 2, as well as the corresponding values of the five dimensionless numbers.

	Parameters: symbols [units]	BIA (Svea in summer)	Ice cave (Eisriesenwelt in winter)	MNPC (summer)	Exp.
		(H_2O ice - air)	(H_2O ice - air)	(H_2O ice - CO_2 atm.)	(CO_2 ice - air)
Flow	Density:	$1.1^{(a)}$	$1.3^{(a)}$	$1.8\times10^{-2(a)}$	$1.2^{(a)}$

	$\rho_f[\mathrm{kg\cdot m^{-3}}]$				
	Kinematic viscosity: $\nu[\mathrm{m^2\cdot s^{-1}}]$	$1.5\times10^{-5(b)}$	$1.3\times10^{-5(b)}$	$6\times10^{-4(b)}$	$1.5\times10^{-5(b)}$
	Friction velocity: $u_*[\mathrm{m\cdot s^{-1}}]$	0.07 [1]	$0.01^{(c)}$	$0.09^{(c)}$ [2,3]	$0.2^{(c)}$
	Boundary layer height: $H[\mathrm{m}]$	70 [4]	4 [5]	10600 [6]	1
Ice	Diffusion coefficient: $D[\mathrm{m^2\cdot s^{-1}}]$	$2.9\times10^{-5(d)}$	$2.4\times10^{-5(d)}$	$1.4\times10^{-3(d)}$	$1.5\times10^{-5(d)}$
	Wavenumber: $k[\mathrm{m^{-1}}]$	31.5 [7]	4.5 [8]	$0.9^{(e)}$	104
	Amplitude: $2\zeta_0[\mathrm{m}]$	$<2\times10^{-2}$ [7]	<0.3 [8]	$<0.5^{(f)}$	$<1\times10^{-2}$
	Sublimation rate: $q^0/\rho_s[\mathrm{m\cdot s^{-1}}]$	$3\times10^{-9(g)}$ [7]	$\le 4.5\times10^{-9(g)}$ [9,10]	$2\times10^{-10(g)}$ [11]	$1.4\times10^{-6(g)}$
Characteristic dimensionless numbers	Schmidt: Sc	0.52	0.54	0.42	1
	Kinetic ratio: $\frac{q^0/\rho_s}{u_*}$	$4.3\times10^{-8}<<1$	$\le 4.5\times10^{-8}<<1$	$2.3\times10^{-9}<<1$	$7\times10^{-6}<<1$
	Relative height: kH	$2100>2\pi$	$18.3>2\pi$	$9540>2\pi$	$104>2\pi$
	Aspect ratio: R_a	<0.10	<0.20	<0.08	<0.16
	Dimensionless wavenumber: $\frac{k\nu}{u_*}$	6.75×10^{-3}	5.85×10^{-3}	6.2×10^{-3}	7.8×10^{-3}

Table 2: Averaged parameters of the problem of sublimation waves formation for the BIA located in Svea, the Eisriesenwelt ice cave, the MNPC and the experimental model. [1] van den Broeke and Bintanja (1995). [2] Forget et al. (1999). [3] Millour et al. (2018). [4] Swain and Gallée (2006). [5] Obleitner and Spötl (2011). [6] Pankine and Tamppari (2015). [7] Bintanja et al. (2001). [8] Curl (1966). [9] Marshall and Brown (1974). [10] Persoiu and Lauritzen (2018). [11] Chittenden et al. (2008). (a) Flow densities are simply derived from the ideal gas law and the environmental conditions of Table 1, assuming that they are not mixed with other gaseous species. (b) Kinematic viscosities are computed from Sutherland's law for the viscosity of gases. (c) Average wind speeds were measured directly and used to deduce friction velocities u_* with a typical law of the wall. (d) The diffusion coefficients are obtained with Boynton's formula (Boynton et al., 2002). (e) The average value of the wavenumber was deduced from the different available HiRISE images of the studied area on the Martian NPC. (f) An upper bound for amplitudes is only given, as indicated in Section 2.3. (g) The sublimation rates were found in the litterature but can be computed from a thermal convection analogy leading to $q^0 / \rho_s = 0.14 \Delta\eta D (\frac{\Delta\rho}{\rho} \frac{g}{\nu^2} \frac{\nu}{D})^{1/3}$, where $\Delta\eta$ is the difference between the a vapor concentration in b at the surface and that of b away from the surface (Ingersoll, 1970; Chittenden et al., 2008; Dundas and Byrne, 2010; Hecht, 2002). The parameters related to the experimental model were computed as described in (a), (b), (c), (d) and (e), or measured directly.

(i) The Schmidt number Sc compares the effects of momentum diffusivity and mass diffusivity in the flow. It is defined as the ratio $Sc = \frac{\nu}{D}$, where ν is the kinematic viscosity of the fluid and D the mass diffusivity. Its order of magnitude is typically 10^3 in liquids while it is closer to 1 in ideal gases, due to much smaller mass diffusivities in liquids (Incropera et al., 2007). The values of Sc in the different environments described in Section 2 differ but are of the same order of magnitude ($Sc \simeq 1$). These values imply momentum and mass transfer diffusivities are comparable, thus the thickness of the concentration boundary layer almost coincides with that of the hydrodynamic boundary layer in all these environments.

(ii) The relative height kH measures the difference in length scale between the turbulent hydrodynamic boundary layer and the sublimation waves. It is defined as $kH = 2\pi \frac{H}{\lambda}$, where H

is the height of the boundary layer and $k = \frac{2\pi}{\lambda}$ is the wavenumber. In all environments described in Section 2, the relative height is such as $kH > 1$, which means that the flow can be considered as "unbounded" in its upper part (Fourrière et al., 2010).

(iii) The aspect ratio R_a is the geometric criterion relating the horizontal and vertical sizes of the waves. It is the ratio $R_a = \frac{2\zeta_0}{\lambda}$ between the amplitude ($2\zeta_0$) and the wavelength of the waves. The maximum values of R_a in all environments described in Section 2 are larger than $R_a \approx 0.03$, the limit above which hydrodynamical non-linear effects are no longer negligible (Kuzan et al., 1989). This point will be discussed in Section 4.1.

(iv) The kinetic ratio compares the kinetics of mass transfer between the solid ice substrate and the fluid with the kinetics of the flow. We define it as $\frac{q^0/\rho_s}{u_*}$, the ratio of the sublimation rate q^0/ρ_s, where q^0 is the matter flux of the base state in the case of an equivalent flat surface and ρ_s the ice density, and the friction velocity of the fluid on the substrate u_*. Its value for all environments described in Section 2 is much less than unity, which indicates that the concentration variations of the sublimated ice into the fluid near the interface are modulated more by the kinetics of the flow than by the sublimation rate (Claudin et al., 2017).

(v) The dimensionless wavenumber controls the near-wall hydrodynamical regime with respect to the waves. It is the inverse of the wavenumber-based Reynolds number and is defined as $\frac{k\nu}{u_*}$, where k is the wavenumber, ν/u_* is the viscous length, ν is the kinematic viscosity of the fluid and u_* is the friction velocity of the fluid on the interface. Three hydrodynamical near-wall regimes can be defined, according to the value of the dimensionless wavenumber: turbulent for $\frac{k\nu}{u_*} < 3\times10^{-4}$, laminar for $2\times10^{-2} < \frac{k\nu}{u_*} < 10^{-1}$ and transitional from laminar to turbulent when $3\times10^{-4} < \frac{k\nu}{u_*} < 2\times10^{-2}$ (Charru et al., 2013). In all environments described in Section 2, its value is close to 7×10^{-3}, meaning that the waves are produced under the transitional near-wall regime.

The wavenumber-based Reynolds number must be differentiated from the global Reynolds number $Re_H = \frac{UH}{\nu}$ based on the height H of the boundary layer, where U is the mean velocity of the flow. $Re_H = \frac{UH}{\nu}$ characterizes the overall flow regime and its value is such as $Re_H \geq 10^5$, which indicates that the boundary layers are turbulent in all environments described in Section 2.

The constant value of the dimensionless wavenumber $\frac{k\nu}{u_*}$ in all environments described in Section 2 suggests that the viscous length ν / u_* is a characteristic length in all natural and experimental environments where sublimation waves have been observed: the viscous length thus appears to be involved in the scaling of the wavelength of sublimation waves. This conclusion is consistent with empirical laws (Thomas, 1979) and dimensional analyses (Blumberg and Curl, 1974), where $\frac{k\nu}{u_*}$ is also constant and stands also in the range of transitional dimensionless wavenumbers.

3.3. Linear stability analysis of the model

To constrain the conditions under which sublimation waves appear, we performed a temporal linear stability analysis on the model described in Section 3.1. A similar stability analysis has been performed and described in details by Claudin et al. (2017). We first briefly review the aims and the methods of this analysis, and then give the results of its adaptation to the sublimation/condensation problem.

3.3.1. Aims

A temporal linear stability analysis aims at examining the temporal stability of a system subject to small disturbances. In our model, the presence of the wavy surface profile produces small disturbances in the atmospheric flow and in the mass transfer between the icy substratum and the flow. We consider these disturbances through the small parameter $k\zeta_0 \propto Ra$. The aim is thus to determine the temporal evolution of a sinusoidal topographic profile of the form:

$$\zeta(x,t) = \zeta_0 e^{\sigma t} \Re(e^{i(kx+\omega t)}), \quad (1)$$

where σ is the temporal growth rate associated to the wavenumber k, and to the angular

frequency ω. From Eq. 1, it appears that σ is responsible for the growth and ω for the propagation of topographic waves with a certain wavenumber k. The waves develop (they are unstable) if $\sigma > 0$, while they fade (they are stable) if $\sigma < 0$. The propagation velocity of the waves is equal to $-\omega / k$ and is thus positive (in the same direction as the wind) if $\omega < 0$ and negative (opposite to the wind) if $\omega > 0$. The linear stability analysis allows to find the dispersion relation $D(\sigma, \omega, k) = 0$ and thus to identify the most unstable wavenumber k, for which the growth rate σ is maximum.

3.3.2. Methods

Linear stability analyses are generally carried out according to the following steps: (i) linearise the governing equations of the model with respect to a small disturbance, (ii) inject the decomposition in normal modes of all quantities into the linearised equations, (iii) derive and solve a system of closed equations with appropriate boundary conditions, (iv) derive the dispersion relation. Given the assumptions of the model (Section 3.1) and its characteristic dimensionless numbers (Section 3.2), these steps, correspond here to:

(i) linearisation of the Reynolds-averaged equations for the flow dynamics and the mass transfer with respect to $k\zeta_0 \propto Ra$, with $Ra < 0.03$;

(ii) injection of the decomposed forms (written as the sum of an homogeneous part and a linear correction with respect to the small parameter) of all quantities (flow speed, stresses, mass flux and concentration) into the linearised equations; definition of characteristic scales (u_* for velocities, ρu_*^2 for stresses, q^0, the base state of the diffusive flux for the flux, and q^0 / u_* for the concentration) to make the quantities dimensionless;

(iii) derivation of closed equations, imposing that the flow is "unbounded" in its upper part at a finite kH and imposing a no-slip condition at $z = \zeta$;

(iv) explicitation of the dispersion relation, after injection of Eq. 1 and decomposition of the flux

$$q = q^0[1 - Fk\zeta_0 e^{\sigma t} e^{i(kx+\omega t)}], \tag{2}$$

into the evolution equation of the interface

$$\rho_s \frac{d\zeta}{dt} = -q(\zeta) + q^0, \tag{3}$$

where F is a non-dimensional mode function, which describes the vertical profile of the linear correction of the flux; the numerical computation of the mode function F and of σ and ω as functions of the dimensionless wavenumber $k\nu/u_*$ to determine the values of this characteristic number for which sublimation waves are unstable.

The last step leads to the dispersion relation:

$$\sigma + i\omega = \frac{q^0}{\rho_s} kF(0), \tag{4}$$

or, by separating the real and imaginary parts:

$$\sigma = \frac{q^0}{\rho_s} k \,|F(0)| \cos\theta_q, \tag{5}$$

$$\omega = \frac{q^0}{\rho_s} k \,|F(0)| \sin\theta_q, \tag{6}$$

The dispersion relation (Eq. 5 and Eq. 6) thus depends explicitly on the flux phase lag θ_q. The phase lag θ_q corresponds to the argument of the complex number $F(0)$, such as $F(0) = |F(0)| e^{i\theta_q}$.

The dimensionless forms σ^+ and ω^+ of the computed dispersion relation are:

$$\sigma^+ = \sigma \frac{\rho_s}{q^0} \frac{\nu}{u_*}, \tag{7}$$

$$\omega^+ = \omega \frac{\rho_s}{q^0} \frac{\nu}{u_*}. \tag{8}$$

[[Image]]

Figure 11: The dispersion relation computed numerically with the model in the $\frac{k\nu}{u_*}$ space, for $Sc = 1$. The absolute value of the dimensionless growth rate σ^+ is represented in (a) and the absolute value of the dimensionless angular frequency ω^+ in (b). The shaded part is the instability domain and corresponds to the unstable wavelengths that can develop. Thin and thick lines represent negative and positive values of σ^+ and ω^+, respectively. The most unstable wavelength k_c^+ corresponds to the largest σ_c^+ and is obtained from (a). By locating k_c^+ on (b),

ω_c^+ and the migration direction can be determined. Pannel (c) illustrates the growth and migration direction of the waves for the most unstable mode. The negative value of ω_c^+ indicates that the waves migrate in the downwind direction ($v = -\omega / k$).

Following Claudin et al. (2017), we compute numerically the linear correction of the mass flux at the interface $F(0)$, which has no explicit expression.

3.3.3. Results: dispersion relation for sublimation waves

To get the dispersion relation for the specific case of sublimation, the stability analysis is performed under the assumptions outlined in the previous sections and by adjusting a specific set of parameters: (i) R_d, the bed roughness-based Reynolds number, introduced by Claudin et al. (2017), is set to 0 (smooth case); (ii) Sc is set to 1, because the values of momentum and mass transfer diffusivities in gas are of the same order of magnitude; (iii) we stay in the limit of a small kinetic ratio (much less than unity), because mass transfers near the interface in the environments described in Section 2 are modulated by the kinetics of the flow, rather than by the sublimation rate. The resulting dispersion relation is displayed on Figure 11 as a function of the dimensionless wavenumber $\frac{k\nu}{u_*}$. The most unstable wavelength is the one which has the largest growth rate σ_c^+ and its associated dimensionless wavenumber is k_c^+ (Figure 11a). Once k_c^+ has been determined, the characteristic angular frequency ω_c^+ and the migration velocity can also be obtained (Figure 11b). The range of k^+ for which the waves are unstable corresponds to the transitional hydrodynamical near-wall regime.

[[Image]]

Figure 12: The phase lag θ_q as a function of $\frac{k\nu}{u_*}$, for $Sc = 0.5$. The phase lag θ_q is defined as the shift between the crest and the maximum of the flux intensity. The unstable waves develop when $90^\circ < \theta_q < 270^\circ$ and when the hydrodynamical near-wall regime is transitional.

For large $\frac{k\nu}{u_*}$ ($\frac{k\nu}{u_*} > 2\times10^{-2}$), when the wavelength is much smaller than the viscous sublayer and the regime is laminar, the regions of largest flux are located slightly upwind of the crests ($0^\circ < \theta_q < 90^\circ$, Figure 12). This is a stabilising situation. For small $\frac{k\nu}{u_*}$ ($\frac{k\nu}{u_*} < 3\times10^{-4}$), in

the turbulent near-wall regime, the maximum flux is located slightly downwind of the crests ($270^\circ < \theta_q < 360^\circ$, Figure 12), and this is a stabilising situation again. Sublimation waves thus cannot develop when $\frac{k\nu}{u_*} > 2\times10^{-2}$ or $\frac{k\nu}{u_*} < 3\times10^{-4}$. For intermediate values of $\frac{k\nu}{u_*}$, corresponding to the transitional near-wall regime, the relaxation on the pressure gradient shifts the maximum flux in the troughs ($90^\circ < \theta_q < 270^\circ$, Figure 12), leading to the destabilisation and growth of the waves.

From the linear stability analysis, the most unstable mode for the formation of sublimation waves can thus be identified in terms of dimensionless wavenumber, growth rate and angular frequency. Those characteristic numbers give a theoretical clue to what should be the wavelength, growth rate, migration velocity, migration direction and characteristic time scales of sublimation waves, if (i) only the most unstable mode develops effectively in nature and (ii) if this mode corresponds to wavelengths and amplitudes large enough to be observed.

3.4. Scaling laws derived from the model

"Loose bedforms" are classicaly used as geomorphic markers of interactions between planetary surfaces and atmospheres. This is possible since scaling laws derived from natural observations, experiments and models are now avalaible, and relate the geometric and kinematic characteristics of loose bedforms to the physical characteristics of their environments (Claudin and Andreotti, 2006; Durán et al., 2011). To provide a similar theoretical framework for interactions of atmospheric flows with icy planetary surfaces, we now derive three scaling laws for sublimation waves. For that purpose, we use the characteristic numbers of the most unstable mode σ_c^+, ω_c^+ and k_c^+, revealed by the dispersion relation. By reworking the set of equations from Eq. 5 to Eq. 8, these characteristic numbers explicitly appear in the expression of the physical quantities (wavelength, migration velocity and characteristic time of formation) that we seek to parameterize.

[[Image]]

Figure 13: Theoretical scaling laws (lines) derived from the dimensionless dispersion relation and superimposed measurements (symbols) from the litterature or from our experiment. Data from sublimation waves on BIAs are represented with blue circles (Bintanja et al., 2001), in ice caves with blue squares (Curl, 1966) and in the experimental model with blue diamonds. Arrows point at

predictions in the different environments. (a) Viscous length $\frac{\nu}{u_*}$ as a function of wavelength λ. (b) Wind speed u_x, transverse to wave crests, as a function of wavelength λ. The height z and the viscosity ν act as parameters for this version of the first law. (c) Migration velocity v as a function of sublimation rate $\frac{q^0}{\rho_s}$. (d) Characteristic formation time t_c of sublimation waves as a function of the ratio viscous length/sublimation rate.

(i) From the dispersion relation expressed in Eq. 5 and Eq. 7, we find a law that links λ to the viscous length $\frac{\nu}{u_*}$:

$$\frac{\nu}{u_*} = \frac{k_c^+}{2\pi}\lambda, \tag{9}$$

where $k_c^+ \simeq 7\times10^{-3}$ is the dimensionless wavenumber, computed numerically, at which the maximum growth rate is reached ($\sigma^+ = \sigma_c^+$). This law (Figure 13a) confirms an empirical law that has been proposed previously from natural and experimental data for different Schmidt numbers (Curl, 1966; Thomas, 1979). It shows that the most unstable wavelength of sublimation waves does not depend on the substrate composition but only on the flow, because this wavelength scales linearly with the viscous length ν / u_*. Wavelengths of sublimation waves can thus be predicted if the viscosity of the atmosphere and the friction velocity are known. This last quantity is difficult to measure, however. Conversely, the viscous length $\frac{\nu}{u_*}$ can be estimated where sublimation waves are detectable and measurable. Thus, the friction velocity can be predicted if the viscosity is known.

The physical significance of the coefficient k_c^+ in the law is not yet clearly identified, but it may depend on the relaxation of the pressure gradient (Hanratty, 1981). No explicit form is found for it and additional work would be necessary to explore its physical meaning.

An alternative form of this law, proposed by Curl (1966) and Ashton and Kennedy (1972) from experimental results, linearly links λ to the inverse of the average wind velocity U. We find that this linear law comes from the logarithmic law:

$$u_x(z) = \frac{u_*}{\kappa} \ln\left(\frac{9 z u_*}{\nu}\right). \quad (10)$$

By injecting Eq. 10 in Eq. 9, we derive the general expression of wind speed $u_x(z)$ at height z as a function of the wavelength λ and the flow viscosity ν:

$$u_x(z) = \frac{2\pi}{k_c^+} \frac{1}{\kappa} \frac{\nu}{\lambda} \ln\left(\frac{18\pi}{k_c^+} \frac{z}{\lambda}\right), \quad (11)$$

where $k_c^+ \simeq 7 \times 10^{-3}$ and $\kappa \simeq 0.41$.

	Parameters	BIA (Svea)	Ice cave (Eisriesenwelt)	MNPC	Exp.
1st law Fig. 13a and 13b	λ(m)	0.22	1.4	7	0.06
	ν / u_*(m)	2.1×10^{-4}	1.3×10^{-4}	7.5×10^{-4}	7.5×10^{-5}
	u_*(m·s^{-1})	0.07	0.01	0.08	0.2
	u_x(m·s^{-1})	2.4 (6 m)	0.2 (1 m)	2.2 (100 m)	6 (1 m)
2nd law Fig. 13c	q^0 / ρ_s(m·s^{-1})	3×10^{-9}	4.5×10^{-9}	2×10^{-10}	1.4×10^{-6}
	ν(m·s^{-1})	8×10^{-9} ≃ 2 cm/month	9×10^{-9} ≃ 2.5 cm/month	4×10^{-10} ≃ 3.5×10^{-2} mm/sol	3×10^{-6} ≃ 10 mm/h
3rd law Fig. 13d	t_c(s)	6.4×10^{6} ≃ 70 days	3×10^{7} ≃ 350 days	3.9×10^{9} ≃ 44000 sols	5.4×10^{3} ≃ 90 min

Table 3: Average values of the parameters involved in the three scaling laws for the different environments (Blue Ice Areas, ice cave, Martian North Polar Cap and experimental model) and displayed on Figure 13. These values correspond to measurements (white cells) or predictions from the laws (grey cells).

In contrast with the first form of the law (Eq. 9), where the friction velocity u_* cannot be measured directly, Eq. 11 relates four quantities (λ, z, ν and u_x), that can be measured in nature (Figure 13b). In the range of heights over which the logarithmic law is valid, this form thus allows to compute the average wind speed at any height above sublimation waves of known

wavelengths, if the viscosity of the flow is known also. The average wind velocity U, corresponding to the wind speed at the top of the turbulent boundary layer, can thus be computed.

(ii) We derive a second scaling law on the migration velocity of sublimation waves. This quantity is found to scale linearly with the average value of the sublimation rate $\frac{q^0}{\rho_s}$, as proposed by Hanratty (1981). From the dispersion relation expressed in Eq. 8 and the definition of the migration velocity $v = |-\omega / k|$, it comes:

$$v = \frac{|\omega_c^+|}{k_c^+}\frac{q^0}{\rho_s}, \tag{12}$$

where $\frac{|\omega_c^+|}{k_c^+} \simeq 2$, according to the numerically computed values of ω_c^+ and k_c^+. The negative value of ω_c^+ (Figure 11b) indicates that sublimation waves must migrate downwind. This law demonstrates that the migration velocity of sublimation waves depends only on the sublimation rate (Figure 13c). It can be used either to predict the migration rate if the sublimation rate is known, or conversely to estimate the sublimation rate, if the migration velocity is known.

(iii) We derive a third law that links the characteristic time of formation of sublimation waves with the viscous length $\frac{\nu}{u_*}$ and the sublimation rate $\frac{q^0}{\rho_s}$ (Figure 13d). From the dispersion relation again, expressed in Eq. 7, and considering $t_c \simeq \frac{1}{\sigma_c}$, we get:

$$t_c = \frac{1}{\sigma_c^+}\frac{\rho_s}{q^0}\frac{\nu}{u_*}, \tag{13}$$

with $\frac{1}{\sigma_c^+} \simeq 100$, according to the numerically computed value of σ_c^+. This last law is a powerful tool to evaluate the development time scale of sublimation wave landscapes, as will be discussed in Section 4.5.

4. Discussion: validation and planetary applications of the scaling laws

4.1. Non-linearity

The first law (Eq. 9) correctly predicts the relation between viscous length and wavelength

observed in natural and experimental sublimation waves (Figure 13a), despite the fact that the aspect ratio of natural sublimation waves is greater than 0.03 (Sections 2.2, 2.3 and 2.4). This suggests that, although non-linear effects may be responsible for morphological changes during the growth of natural sublimation waves, the linear expansion of the problem is still reasonable. Possible morphological changes due to non-linear effects include development of asymmetric profiles and large aspect ratios in natural sublimation waves.

4.2. Importance of the turbulence model

The model by Bintanja et al. (2001) was not designed to identify the maximal growth rate of sublimation waves and therefore, their most unstable mode. This model thus provides only an upper bound for the wavelength, such as $\lambda < 16\,\mathrm{cm}$, suggesting that all wavelengths smaller than this limit can develop. This bound of the wavelength is slightly lower than our predicted wavelength ($20\,\mathrm{cm}$), but is of the same order of magnitude. Bintanja's model fails at predicting correctly the migration direction of sublimation waves. The main difference between the two models lies in the type of turbulent closure. To model properly the feedback between the flow and the topography, the classical Van Driest's mixing length is not sufficient and needs to be adapted with a specific relaxation on the pressure gradient (Hanratty, 1981).

4.3. A comparison tool for wind and climate models

Wind velocity measurements are performed in nature at various heights z. To compare these values with our predictions, we use Eq. 11 with a set of parameters ($\nu = 1.5\times10^{-5}\,\mathrm{m^2\cdot s^{-1}}, z = 6\,\mathrm{m}$ for BIAs, $\nu = 1.5\times10^{-5}\,\mathrm{m^2\cdot s^{-1}}, z = 1\,\mathrm{m}$ for ice caves and $\nu = 1.3\times10^{-5}\,\mathrm{m^2\cdot s^{-1}}$, $z = 1\,\mathrm{m}$ for the experiment). The theoretical results are in good agreement with the measurements (Figure 13b). The law does not depend strongly on the height z, as the predictions are really close for $z = 1\,\mathrm{m}$ and $z = 6\,\mathrm{m}$, for the same viscosity (BIA and experimental model, respectively).

The first scaling law (Eq. 9) applied to the Martian North Polar Cap leads to a predicted friction velocity $u_* \approx 0.09\,\mathrm{m\cdot s^{-1}}$ in the area described in Section 2.3. By using daily average horizontal wind speeds for solar longitudes between 110° and 120° from the GCM simulations of the Mars Climate DataBase (MCD) (Forget et al., 1999; Millour et al., 2018) as an input for the typical law of the wall for dynamically smooth flow, we obtained a friction velocity of

$u_* \approx 0.08\,\mathrm{m\cdot s^{-1}}$, which is in good agreement with this prediction. The similarity of friction velocities induces the similarity of wind speed profiles. For example, at a height $z = 100\,\mathrm{m}$, the wind speed is predicted to be $u_x(100\,\mathrm{m}) = 2.2\,\mathrm{m\cdot s^{-1}}$ with Eq. 11, while the daily average wind speed provided by the MCD simulation is $u_x(\mathrm{m}) = 2.5\ \mathrm{m\cdot s^{-1}}$ (Forget et al., 1999; Millour et al., 2018). The first law (Eq. 9 and Eq. 11) is therefore a powerful tool for the validation of wind and climate models. This result also supports our suggestion that the linear ridges observed on the MNPC are sublimation waves. Other tests should be performed on different locations of the MNPC where small-scale features exist (Nguyen et al., 2020) to consider the possibility that these landforms are sublimation waves.

4.4. Migration velocity

The maximum observed migration velocity of sublimation waves in BIAs is $2\,\mathrm{cm/month}$ in the downwind direction (Bintanja et al., 2001). The second scaling law (Eq. 12) predicts a migration velocity of $1.6\,\mathrm{cm/month}$ in the downwind direction from the measured sublimation rate (Table 2), which is in excellent agreement with the observations. This is the only point of comparison available, since no estimations for ice caves and the Martian North Polar Cap were found in the literature.

With the second law (Eq. 12), we find a migration velocity of $2.5\,\mathrm{cm/month}$ of sublimation in the Eisriesenwelt ice cave, assuming a maximal sublimation rate of the order or $5\times10^{-9}\,\mathrm{m\cdot s^{-1}}$ (Persoiu and Lauritzen, 2018). These waves should thus have a displacement on the order of $7\,\mathrm{cm}$ in winter. The predicted migration velocity for the sublimation waves in the experiment is $10\,\mathrm{mm/h}$. In these two latter cases, the predicted values are realistic and could be confirmed by future measurements. On the MNPC, the migration is predicted to be very slow (3.5×10^{-2} mm/sol of sublimation). If we consider that the sublimation waves migrate during all the water ice sublimation period ($\approx 20^\circ$ in solar longitude, which corresponds to $37\,\mathrm{sols}$), then their total displacement in a entire Martian year should be less than $2\,\mathrm{mm}$. This low value is consistent with the fact that no migration of these waves can be observed over a 13 years interval on HiRISE images with a resolution of $25\,\mathrm{cm/pixel}$ (Section 2.3).

4.5. Characteristic time of formation

According to our analysis, the characteristic time of formation of sublimation waves is much larger than the time scale of turbulence, which justifies the use of averaged quantities when modeling. In BIAs, this characteristic time is estimated to be about 70 days (as computed from their increase in height during summer (Bintanja et al., 2001)). This duration is consistent with the value of 85 days computed from the third scaling law's (Eq. 13). In the experiment, sublimation waves developed in less than 4 hours, which is also in agreement with the predicted time of $90\,\mathrm{min}$.

We find that the development time scale of sublimation waves in the Eisriesenwelt ice cave is approximately $350\,\mathrm{days}$ of sublimation, with a sublimation rate on the order of $5\times10^{-9}\,\mathrm{m\cdot s^{-1}}$ in winter (Persoiu and Lauritzen, 2018). It means that a few years should be necessary to make them visible on the walls of ice caves. On the MNPC, this time is predicted to be approximately $44000\,\mathrm{sols}$ of sublimation, which is equivalent to approximately 1200 Martian years. This time scale is too long to observe the emergence of new sublimation waves in the near future. In order to evaluate the possibility for such waves to grow within the predicted time we compare this with the time scale of formation of the MNPC. If the MNPC likely formed during the last $5\,\mathrm{Myr}$ (Hvidberg et al., 2012), an upper bound for the age of the uppermost layer is believed to be about $300\,\mathrm{kyr}$ (Head et al., 2003), which corresponds to the last change of Mars obliquity. Assuming that the water cycle was comparable during that time to the one observed today, we evaluate that water ice of the MNPC experienced sublimation during 5.5% of the period, corresponding to $\simeq 17000$ Martian years. Therefore the predicted characteristic time to form sublimation waves is consistent with the MNPC time scale and suggests that the area in which sublimation waves are visible has sustained sublimation for thousands of Martian years.

The characteristic time is a powerful tool to predict sublimation rates. As they are still poorly constrained in ice caves and measured with difficulty on terrestrial and Martian ice sheets, sublimation rates could be estimated by monitoring the average time scale of development of sublimation waves.

4.6. What about condensation waves?

[[Image]]

Figure 14: The dispersion relation computed numerically with the model in the $\frac{k\nu}{u_*}$ space in the

case of condensation. The absolute value of the dimensionless growth rate σ^+ is represented in (a) and the absolute value of the dimensionless angular frequency ω^+ in (b). The shaded part is the instability domain and corresponds to the unstable wavelengths that can develop. Thin and thick lines represent negative and positive values of σ^+ and ω^+, respectively. The most unstable wavelength k_c^+ corresponds to the largest σ_c^+ and is obtained from (a). By locating k_c^+ on (b), ω_c^+ and the migration direction can be determined. Pannel (c) illustrates the growth and migration direction of the waves for the most unstable mode in the turbulent near-wall regime. The negative value of ω_c^+ indicates that the waves migrate in the downwind direction ($v = -\omega / k$). Pannel (d) illustrates the growth and migration direction of the waves for the most unstable mode in the laminar near-wall regime. The positive value of ω_c^+ indicates that the waves migrate in the upwind direction.

Under appropriate pressure, temperature and humidity conditions, atmospheric vapors can condense in the form of frost on solid substrates. This is a classical ice accumulation process on the Earth and it has been proposed to occur also on several other bodies of the Solar Sytem, such as Venus (Schaefer and Jr, 2004), the Moon (Hayne et al., 2015), Mars (Ivanov and Muhleman, 2000), Callisto (Lebofsky, 1977), Pluto and Charon (Cruikshank et al., 1976; Buie et al., 1987) and comets (De Sanctis et al., 2015). To our knowledge, topographic waves formed by condensation of atmospheric vapors in windy atmospheres have never been observed on the Earth or elsewhere. The model described in Sections 3, according to the assumptions of Sections 3.1 and 3.2, can therefore be used to evaluate the theoretical possibility that such "condensation waves" could exist in environments similar to those described in Section 2 or determine the conditions under which their development would be possible elsewhere.

The only difference with sublimation is that the flux is oriented in the opposite direction (the sign changes in front of q in Eq. 3), leading to an opposite dispersion relation, by injecting Eq. 1 and Eq. 2 into Eq. 3 (Figure 14a and 14b). The destabilising situations for condensation thus correspond to large $\frac{k\nu}{u_*}$ (laminar near-wall regime) and small $\frac{k\nu}{u_*}$ (turbulent near-wall regime), while the transitional regime remains stable. The dimensionless wavenumber of the most unstable wavelength k_c^+ occurs in the laminar near-wall regime and is three to four orders of magnitude greater for condensation than for sublimation. The wavelength of condensation waves in this

regime is thus expected to be four orders of magnitude smaller than that of sublimation waves under similar conditions for u_* and ν. Under the conditions of BIAs in Antarctica, ice caves, the MNPC and our experimental model, wavelengths generated by condensation would be very small: 10^{-4} m, 8×10^{-4} m, 4×10^{-3} m and 4×10^{-5} m, respectively. Condensation waves of this size would not be visible at all and hardly detectable, even if they existed in those environments. To generate condensation waves of visible size in the laminar near-wall regime, the viscous length should be larger, involving larger viscosities of the atmosphere or smaller friction velocities. These conditions may perhaps occur on other planetary bodies. In the turbulent regime, wavelengths of condensation waves are expected to be one to two orders of magnitude greater than for sublimation. Natural examples of such condensation waves have not been described yet, but could exist.

The predicted difference in wavelengths of topographic waves produced by either sublimation or condensation, may help differentiate these two possible formation processes in natural settings. In addition, internal layering of the substrate should be expected for condensation waves, because they would develop by progressive accumulation of ice crystal layers at their surface. By contrast, the development of sublimation waves is unable to produce such internal layering because sublimation is an ablative process. On the Earth and other bodies of the Solar System, internal layering of icy substrates may be observed in-situ or by remote-sensing, either directly in vertical outcrops, or indirectly on vertical profiles provided by subsurface sounding radars (e.g., Frezzotti et al. (2002); Christian et al. (2013); Herny et al. (2014)). Sublimation and condensation areas on terrestrial ice sheets and other icy planetary surfaces can also be differentiaded from remotely-sensed spectroscopic observations (e.g., Herny et al. (2014)) or from external constrains, derived either from measurements or from models, on the relative humidity and temperature of the atmosphere during the development of the observed topographic waves.

5. Conclusions

[[Image]]

Figure 15: Formation of sublimation waves under a turbulent boundary layer flow. The initial ice-flow interface may display irregularities such as bumps and depressions. The instability caused by the hydrodynamical anomaly in the transitional near-wall regime and the diffusion processes, leads to the growth and selection of, after a characteristic time scale t_c, a specific wavelength λ

that migrates with a velocity v. The flow speed $u_x(z)$ at height z is related to the wavelength. The coefficients k_c^+, ω_c^+ and σ_c^+ come from the results of the linear stability analysis and correspond to the dimensionless wavenumber, angular frequency and growth rate of the most unstable mode, respectively.

Sublimation waves are linear and periodic bedforms resulting from an instability at the interface between an icy substrate and a turbulent boundary layer flow. Observations on Earth (BIAs and ice caves), Mars (North Polar Cap), and in a wind tunnel experiment reveal that sublimation waves appear and develop in specific environments, such as in dry and cold areas where the partial vapour pressure of the sublimating ice is far enough from the corresponding saturated vapour pressure. The sublimating vapour diffuses into the gas that composes the flow, which is globally turbulent. The crests of sublimation waves are linear, parallel and transverse to the main wind direction. Their wavelength λ varies from an environment to another (for example, $\lambda \simeq 20\,\mathrm{cm}$ in BIAs and $\lambda \simeq 7\,\mathrm{m}$ on the MNPC) and their height $2\zeta_0$ also ($2\zeta_0 \simeq 1\,\mathrm{cm}$ and $2\zeta_0 \simeq 50\,\mathrm{cm}$, respectively). The crests migrate in the downwind direction and form under a characteristic time.

Sublimation waves formation involves several characteristics of both the icy substrate and the flow. In currently known natural and experimental occurences, the length scale of the hydrodynamical boundary layer is larger than the sublimation waves length scale. The height of the concentration boundary layer is close to that of the hydrodynamical boundary layer. The kinematics of the flow control the concentration of vapour above the surface. Non-linear effects may be involved in their development but these effects do not alter significantly the wavelength that appears in the linear phase.

Sublimation waves are produced under the transitional near-wall regime, which induces a strong feedback between the bedforms and the flow. It means that sublimation waves can grow only if $3\times10^{-4} < \dfrac{k\nu}{u_*} < 2\times10^{-2}$, where k is the wavenumber, ν the viscosity of the fluid and u_* the friction velocity. The wavelength is thus controlled by the viscous length ν/u_*. The transitional regime needs a specific modelization of the turbulent viscosity, which cannot be taken as constant. Only a relaxation on the pressure gradient included in the Van Driestâ€™s mixing length leads to correct modeling of the matter transfer.

To our knowledge, ”condensation waves”, i.e. topographic waves produced by condensation of vapor on solid substrates, have never been described on Earth or other planetary bodies. Our analysis however demonstrates that this kind of bedforms can develop theoretically in two near-wall hydrodynamic regimes. In the laminar regime, they would be so small that they probably couldn't be observed. In the turbulent regime however, their sizes would be several orders of magnitude larger than those of sublimation waves: future investigations may reveal their existence on terrestrial ice sheets and extraterrestrial planetary surfaces.

From our analyses, three scaling laws ((i), (ii) and (iii) on Fig. 15) were derived, which can be applied to both sublimation and condensation cases. They link the main morphological and kinematic features (wavelength λ, migration velocity v and time scale of development t_c) of the waves to the surrounding environmental conditions (flow viscosity ν, wind speed u_x, sublimation rate q^0 / ρ_s). They were tested for sublimation waves on several examples on Earth (BIAs in Antarctica, ice caves and an experimental model) and on the Martian North Polar Cap, and validated for all the cases for which measurements were available. This application shows that the scaling laws can be used to predict or estimate parameters such as friction velocities u_*, wind speeds at any height z, wind directions, migration velocities, sublimation rates or characteristic time of formation of sublimation waves in environments where sublimation occurs. As sublimation is expected on other icy planetary surfaces, the scaling laws constitute powerful tools for the prediction of those quantities there. As geomorphic markers, sublimation waves constitute a complementary database to loose aeolian bedforms, allowing a new kind of validation of atmospheric, climatic and wind numerical models over ice sheets and other icy substrates.

Pluto seems to be a good candidate for possible future applications, as sublimation and persistent winds have been suspected to play a role in shaping its surface (Moore et al., 2018). But more widely, the existence of sublimation waves may also be expected on all planetary bodies where surface ices is exposed to flowing gaseous fluids, like the Moon, Ceres and the icy moons of Jupiter and Saturn.

Funding

We acknowledge financial support from the Centre National de la Recherche Scientifique (CNRS)/INSU, through the TelluS Program ”Caractérisation et modélisation des formes de dissolution périodiques sur les parois calcaires soumises à des écoulements d'eau” project and

through the MI In*FI*niti ”Effets liés au changement de phase sur la stabilité et la forme des interfaces glacées en présence d’un écoulement atmosphérique turbulent” project. We also acknowledge financial support from the University of Nantes, the CNRS and Région Pays de la Loire, through the GeoPlaNet project and the Programme National de Planétologie (PNP) through the ”Modélisation de la sublimation comme agent géomorphologique à la surface des planètes” project.

Acknowledgement

We specially thank Clément Blanchard for his contribution to the initial project and two anonymous referees for their constructive comments.

This work	Claudin et al. (2017)
ρ_f	ρ
ζ	z
ζ_0	ζ
Sc	β_ν
q^0	q_0
σ_c^+	σ_m
k_c	k_m

Table A.4: Notation correspondence between our work and Claudin et al. (2017).

Appnedix A. Notation correspondence

References

Allen, J., 1982. Sedimentary structures, their character and physical basis. Number 30 in Developments in Sedimentology, Elsevier.

Ashton, G., Kennedy, J., 1972. Ripples on the underside of river ice covers. Journal of Hydraulic Engineering 98, 1603–1624.

Ashton, G.D., 1972. Turbulent heat transfer to wavy boundaries. Proc. Heat Transfer Fluid Mech. Inst.

Barr, A.C., Milkovich, S.M., 2008. Ice grain size and the rheology of the martian polar deposits.

Icarus 194, 513–518. doi: 10.1016/j.icarus.2007.11.018.

Bella, P., 2007. Morphology of ice surfaces in the Dobšiná Ice Cave, in: Proceedings of the 2nd International Workshop on Ice Caves.

Bertrand, T., Forget, F., Umurhan, O.M., Grundy, W.M., Schmitt, B., Protopapa, S., Zangari, A.M., White, O.L., Schenk, P.M., Singer, K.N., Stern, A., Weaver, H.A., Young, L.A., Ennico, K., Olkin, C.B., 2018. The nitrogen cycles on Pluto over seasonal and astronomical timescales. Icarus 309, 277–296. URL: doi:10.1016/j.icarus.2018.03.012, doi: 10.1016/j.icarus.2018.03.012.

Bintanja, R., 1999. On the Glaciological, Meteorological, and Climatological Significance of Antarctic Blue Ice Areas. Reviews of Geophysics 37, 337–359. doi: 10.1029/1999RG900007.

Bintanja, R., Reijmer, C.H., Hulscher, S.J., 2001. Detailed observations of the rippled surface of Antarctic blue-ice areas. Journal of Glaciology 47, 387–396. URL: http://www.ingentaconnect.com/content/igsoc/jog/2001/00000047/00000158/art00005, doi: 10.3189/172756501781832106.

Bintanja R., V.D.B.M., 1995. The surface energy balance of antartic snow and blue ice. Journal of Applied Meteorology 34, 902–926. doi: 10.1175/1520-0450(1995)034 < 0902:TSEBOA > 2.0.CO;2.

Blumberg, D., Greeley, R., 1996. A Comparison of General Circulation Model Predictions to Sand Drift and Dune Orientations. Journal of Climate 9, 3248–3259. doi: 10.1175/1520-0442(1996)009 < 3248:ACOGCM > 2.0.CO;2.

Blumberg, P.N., Curl, R.L., 1974. Experimental and Theoretical Studies of Dissolution Roughnesses. Journal of Fluid Mechanics 65, 735–751. doi: 10.1017/S0022112074001625.

Bourke, M.C., Lancaster, N., Fenton, L.K., Parteli, E.J., Zimbelman, J.R., Radebaugh, J., 2010. Extraterrestrial dunes: An introduction to the special issue on planetary dune systems. Geomorphology 121, 1–14. URL: http://dx.doi.org/10.1016/j.geomorph.2010.04.007, doi: 10.1016/j.geomorph.2010.04.007.

Boynton, W.V., Feldman, W.C., Squyres, S.W., Prettyman, T.H., Brückner, J., Evans, L.G., Reedy, R.C., Starr, R., Arnold, J.R., Drake, D.M., Englert, P.A., Metzger, A.E., Mitrofanov, I., Trombka, J.I., D'Uston, C., Wänke, H., Gasnault, O., Hamara, D.K., Janes, D.M., Marcialis, R.L., Maurice, S., Mikheeva, I., Taylor, G.J., Tokar, R., Shinohara, C., 2002. Distribution of Hydrogen in the Near Surface of Mars: Evidence for Subsurface Ice Deposits. Science 297,

81–85. doi: 10.1126/science.1073722.

van den Broeke, M.R., Bintanja, R., 1995. Summertime atmospheric circulation in the vicinity of a blue ice area in East Queen Maud Land Antarctica. Boundary-Layer Meteorology 72, 411–438. doi: 10.1007/BF00709002.

Brown, A.J., Calvin, W.M., Becerra, P., Byrne, S., 2016. Martian north polar cap summer water cycle. Icarus 277, 401–415. URL: http://dx.doi.org/10.1016/j.icarus.2016.05.007, doi: 10.1016/j.icarus.2016.05.007.

Buie, M., Cruikshank, D.P., Lebofsky, L., 1987. Water frost on Charon. Nature 329, 522–523. doi: 10.1038/329522a0.

Camporeale, C., Ridolfi, L., 2012a. Hydrodynamic-Driven Stability Analysis of Morphological Patterns on Stalactites and Implications for Cave Paleoflow Reconstructions. Physical Review Letters 108, 1–5. doi: 10.1103/PhysRevLett.108.238501.

Camporeale, C., Ridolfi, L., 2012b. Ice ripple formation at large Reynolds numbers. Journal of Fluid Mechanics 694, 225–251. doi: 10.1017/jfm.2011.540.

Chan, P.Y., Goldenfeld, N., 2007. Steady states and linear stability analysis of precipitation pattern formation at geothermal hot springs. Physical Review E 76. doi: 10.1103/PhysRevE.76.046104.

Charnay, B., Barth, E., Rafkin, S., Narteau, C., Lebonnois, S., Rodriguez, S., Courrech Du Pont, S., Lucas, A., 2015. Methane storms as a driver of Titan's dune orientation. Nature Geoscience 8, 362–366. doi: 10.1038/ngeo2406.

Charru, F., Andreotti, B., Claudin, P., 2013. Sand Ripples and Dunes. Annual Review of Fluid Mechanics 45, 469–493. URL: http://www.annualreviews.org/doi/10.1146/annurev-fluid-011212-140806, doi: 10.1146/annurev-fluid-011212-140806.

Chassaing, P., 2000. Turbulence en mécanique des fluides. Cépaduès.

Chittenden, J.D., Chevrier, V., Roe, L.A., Bryson, K., Pilgrim, R., Sears, D.W.G., 2008. Experimental study of the effect of wind on the stability of water ice on Mars. Icarus 196, 477–487. doi: 10.1016/j.icarus.2008.01.016.

Christian, S., Holt, J.W., Byrne, S., Fishbaugh, K.E., 2013. Integrating radar stratigraphy with high resolution visible stratigraphy of the north polar layered deposits, Mars. Icarus 226, 1241–1251. URL: http://dx.doi.org/10.1016/j.icarus.2013.07.003, doi:

10.1016/j.icarus.2013.07.003.

Cigna, A., Forti, P., 2012. The speleogenetic role of air flow caused by convection. 1st contribution. International Journal of Speleology 15, 41–52. doi: 10.5038/1827-806x.15.1.3.

Claudin, P., Andreotti, B., 2006. A scaling law for aeolian dunes on Mars, Venus, Earth, and for subaqueous ripples. Earth Planet. Sci. Lett. 252, 30–44. URL: http://dx.doi.org/10.1016/j.epsl.2006.09.004, doi: 10.1016/j.epsl.2006.09.004.

Claudin, P., Durán, O., Andreotti, B., 2017. Dissolution instability and roughening transition. Journal of Fluid Mechanics 832, 832R21–832R214. doi: 10.1017/jfm.2017.711.

Cohen-Zada, A.L., Blumberg, D.G., Maman, S., 2016. Earth and planetary aeolian streaks: A review. Aeolian Research 20, 108–125. URL: http://dx.doi.org/10.1016/j.aeolia.2015.12.002, doi: 10.1016/j.aeolia.2015.12.002.

Consolmagno, G.J., Lewis, J.S., 1978. The Evolution of Icy Satellite Interiors and Surfaces. Icarus 34, 280–293. doi: 10.1016/0019-1035(78)90168-9.

Cooke, R.U., Warren, A., Goudie, A.S., 1993. Desert Geomorphology. CRC Press. URL: https://books.google.fr/books?id=WOcUNbKUGtwC.

Courrech du Pont, S., 2015. Dune morphodynamics. Comptes Rendus Physique 16, 118–138. URL: http://dx.doi.org/10.1016/j.crhy.2015.02.002, doi: 10.1016/j.crhy.2015.02.002.

Craddock, R.A., 2012. Aeolian processes on the terrestrial planets: Recent observations and future focus. Progress in Physical Geography 36, 110–124. doi: 10.1177/0309133311425399.

Cruikshank, D.P., Pilcher, C.B., Morrison, D., 1976. Pluto: Evidence for Methane frost. Science 194, 835—-837. doi: 10.1126/science.194.4267.835.

Curl, R.L., 1966. Scallops and flutes. Transactions Cave Research Group of Great Britain 7, 121–160. URL: http://izrk2.zrc-sazu.si/index.php?mact=ShopMadeSimple,cntnt01,fe_product_detail,0&cntnt01display=productlist&cntnt01lang=en_US&cntnt01category_id=&cntnt01pagenumber=1114&cntnt01returnid=17&cntnt01product_id=12257&cntnt01returnid=17.

Cutts, J.a., Blasius, K.R., Roberts, W.J., 1979. Evolution of Martian Polar Landscapes: Interplay of Long-Term Variations in Perennial Ice Cover and Dust Storm Intensity. Journal of Geophysical Research 84, 2975. URL: http://www.agu.org/pubs/crossref/1979/JB084iB06p02975.shtml, doi: 10.1029/JB084iB06p02975.

De Sanctis, M.C., Capaccioni, F., Ciarniello, M., 2015. The diurnal cycle of water ice on comet 67P/ChuryumovGerasimenko. Nature 525, 500–503. doi: 10.1038/nature14869.

Douté, S., Jiang, C., 2019. Small-Scale Topographical Characterization of the Martian Surface With In-Orbit Imagery. IEEE Transactions on Geoscience and Remote Sensing 58, 447–460. doi: 10.1109/TGRS.2019.2937172.

Dundas, C.M., Byrne, S., 2010. Modeling sublimation of ice exposed by new impacts in the martian mid-latitudes. Icarus 206, 716–728. URL: http://dx.doi.org/10.1016/j.icarus.2009.09.007, doi: 10.1016/j.icarus.2009.09.007.

Durán, O., Andreotti, B., Claudin, P., Winter, C., 2019. A unified model of ripples and dunes in water and planetary environments. Nature Geoscience 12, 345–350. URL: http://dx.doi.org/10.1038/s41561-019-0336-4, doi: 10.1038/s41561-019-0336-4.

Durán, O., Claudin, P., Andreotti, B., 2011. On aeolian transport: Grain-scale interactions, dynamical mechanisms and scaling laws. Aeolian Research 3, 243–270. doi: 10.1016/j.aeolia.2011.07.006.

Edgett, K.S., Williams, R.M.E., Malin, M.C., Cantor, B.A., Thomas, P.C., 2003. Mars landscape evolution: influence of stratigraphy on geomorphology in the north polar region 52, 289–297. doi: 10.1016/S0169-555X(02)00262-3.

Fanale, F., Postawko, S., Pollack, J., Carr, M., Pepin, R., 1992. Mars - Epochal climate change and volatile history, in: Kieffer, H., Jakosky, B., Snyder, C., Matthews, M. (Eds.), Mars, pp. 1135–1179.

Fenton, L.K., Hayward, R.K., 2010. Southern high latitude dune fields on Mars: Morphology, aeolian inactivity, and climate change. Geomorphology 121, 98–121. URL: http://dx.doi.org/10.1016/j.geomorph.2009.11.006, doi: 10.1016/j.geomorph.2009.11.006.

Fenton, L.K., Richardson, M.I., 2001. Martian surface winds: Insensitivity to orbital changes and implications for aeolian processes. Journal of Geophysical Research E: Planets 106, 32885–32902. doi: 10.1029/2000JE001407.

Fenton, L.K., Toigo, A.D., Richardson, M.I., 2005. Aeolian processes in Proctor Crater on Mars: Mesoscale modeling of dune-forming winds. Journal of Geophysical Research E: Planets 110, 1–18. doi: 10.1029/2004JE002309.

Fisher, D.A., 1993. If Martian Ice caps Flow: Ablation Mechanisms and Appearance. Icarus 105, 501–511. URL:

http://www.gfy.ku.dk/ddj/MarsDavid.pdf%5Cnhttp://linkinghub.elsevier.com/retrieve/doi/10.1006/icar.1993.1144, doi: 10.1006/icar.1993.1144.

Ford, D.C., Williams, P., 1989. Karst geomorphology and Hydrology. Springer Netherlands.

Forget, F., Hourdin, F., Dalagrand, O., 1999. Improved general circulation models of the Martian atmosphere from the surface to above 80 km. Journal of Geophysical Research – Planets (E) 104, 24,155–24,175. doi: 10.1029/1999JE001025.

Formisano, M., De Sanctis, M.C., Magni, G., Federico, C., Capria, M.T., 2016. Ceres water regime: surface temperature, water sublimation and transient exo(atmo)sphere. Monthly Notices of the Royal Astronomical Society 455, 1892–1904. doi: 10.1093/MNRAS/STV2344.

Fourrière, A., Claudin, P., Andreotti, B., 2010. Bedforms in a turbulent stream: formation of ripples by primary linear instability and of dunes by non-linear pattern coarsening. Journal of Fluid Mechanics 649, 287–328. URL: http://www.journals.cambridge.org/abstract_S0022112009993466%5Cnhttp://dx.doi.org/10.1017/s0022112009993466, doi: 10.1017/S0022112009993466.

Fretwell, P., Pritchard, H.D., Vaughan, D.G., Bamber, J.L., Barrand, N.E., Bell, R., Bianchi, C., Bingham, R.G., Blankenship, D.D., Casassa, G., Catania, G., Callens, D., Conway, H., Cook, A.J., Corr, H.F., Damaske, D., Damm, V., Ferraccioli, F., Forsberg, R., Fujita, S., Gim, Y., Gogineni, P., Griggs, J.A., Hindmarsh, R.C., Holmlund, P., Holt, J.W., Jacobel, R.W., Jenkins, A., Jokat, W., Jordan, T., King, E.C., Kohler, J., Krabill, W., Riger-Kusk, M., Langley, K.A., Leitchenkov, G., Leuschen, C., Luyendyk, B.P., Matsuoka, K., Mouginot, J., Nitsche, F.O., Nogi, Y., Nost, O.A., Popov, S.V., Rignot, E., Rippin, D.M., Rivera, A., Roberts, J., Ross, N., Siegert, M.J., Smith, A.M., Steinhage, D., Studinger, M., Sun, B., Tinto, B.K., Welch, B.C., Wilson, D., Young, D.A., Xiangbin, C., Zirizzotti, A., 2013. Bedmap2: improved ice bed, surface and thickness datasets for Antarctica. Cryosphere 7, 375–393. doi: 10.5194/tc-7-375-2013.

Frezzotti, M., Gandolfi, S., Urbini, S., 2002. Snow megadunes in Antarctica: Sedimentary structure and genesis. Journal of Geophysical Research Atmospheres 107, 1–12. doi: 10.1029/2001JD000673.

Gilpin, R.R., Hirata, T., Cheng, K., 1980. Wave formation and heat transfer at an ice-water interface in the presence of a turbulent flow. Journal Of Fluid Mechanics 99, 619–640. URL: http://www.google.com/search?client=safari&rls=en-us&q=waveformation_Gilpin&ie=UTF

-8&oe=UTF-8%5Cnpapers2://publication/uuid/C424312D-4C90-4DBE-B895-67090DB4774D, doi: 10.1017/S0022112080000791.

Giovinotto, M.B., 1964. Distribution of diagenetic snow facies in Antarctica and in Greenland. Arctic 17, 32–40. doi: 10.14430/arctic3482.

Goodchild, M., Ford, D.C., 1972. Analysis of Scallop Patterns by Simulation Under Controlled Conditions. The Journal of Geology 80, 121–122. doi: 10.1086/627717.

Greeley, R., Bender, K., Saunders, R., Schubert, G., Weitz, C., 1997. Aeolian Processes and Features on Venus, in: Venus II: Geology, Geophysics, Atmosphere, and Solar Wind Environment. University of Arizona Press, p. 547.

Greeley, R., Skypeck, A., Pollack, J.B., 1993. Martian Aeolian Features and Deposits: Comparisons With General Circulation Model Results. Journal of Geophysical Research 98, 3183–3196. doi: 10.1029/92JE02580.

Hanratty, T.J., 1981. Stability of Surfaces That Are Dissolving or Being Formed by Convective Diffusion. Annual Review of Fluid Mechanics 13, 231–252. doi: 10.1146/annurev.fl.13.010181.001311.

Hayne, P.O., Hendrix, A., Sefton-Nash, E., Siegler, M.A., Lucey, P.G., Retherford, K.D., Williams, J.P., Greehagen, B.T., Paige, D.A., 2015. Evidence for exposed water ice in the Moon's south polar regions from Lunar Reconnaissance Orbiter ultraviolet albedo and temperature measurements. Icarus 255, 58–69. doi: 10.1016/j.icarus.2015.03.032.

Hayward, R.K., Mullins, K.F., Fenton, L.K., Hare, T.M., Titus, T.N., Bourke, M.C., Colaprete, A., Christensen, P.R., 2007. Mars Global Digital Dune Database and initial science results. Journal of Geophysical Research E: Planets 112, 1–17. doi: 10.1029/2007JE002943.

Head, J.W., Mustard, J.F., Kreslavsky, M.A., Milliken, R.E., Marchant, D.R., 2003. Recent ice ages on Mars. Nature 426, 797–802. doi: 10.1038/nature02114.

Hecht, M.H., 2002. Metastability of Liquid Water on Mars. Icarus 156, 373–386. doi: 10.1006/icar.2001.6794.

Herny, C., Massé, M., Bourgeois, O., Carpy, S., Le Mouélic, S., Appéré, T., Smith, I.B., Spiga, A., Rodriguez, S., 2014. Sedimentation waves on the Martian North Polar Cap: Analogy with megadunes in Antarctica. Earth and Planetary Science Letters 403, 56–66. URL: http://dx.doi.org/10.1016/j.epsl.2014.06.033, doi: 10.1016/j.epsl.2014.06.033.

Hofstadter, M.D., Murray, B.C., 1990. Ice Sublimation and Rheology: Implications for the

Martian Polar Layered Deposits. Icarus 84, 352–361. doi: 10.1016/0019-1035(90)90043-9.

Holt, J.W., Fishbaugh, K.E., Byrne, S., Christian, S., Tanaka, K., Russell, P.S., Herkenhoff, K.E., Safaeinili, A., Putzig, N.E., Phillips, R.J., 2010. The construction of Chasma Boreale on Mars. Nature 465, 446–449. URL: http://dx.doi.org/10.1038/nature09050, doi: 10.1038/nature09050.

Howard, A.D., 2000. The Role of Eolian Processes in Forming Surface Features of the Martian Polar Layered Deposits. Icarus 144, 267–288. doi: 10.1006/icar.1999.6305.

Howard, A.D., Cutts, J.A., Blasius, K.R., 1982. Stratigraphic Relationships within Martian Polar Cap Deposits. Icarus 50, 161–215. doi: 10.1016/0019-1035(82)90123-3.

Howard, A.D., Moore, J.M., 2008. Sublimation-driven erosion on Callisto: A landform simulation model test. Geophysical Research Letters 35, 2–5. doi: 10.1029/2007GL032618.

Hui, F., Ci, T., Cheng, X., Scambo, T.A., Liu, Y., Zhang, Y., Chi, Z., Huang, H., Wang, X., Wang, F., Zhao, C., Jin, Z., Wang, K., 2014. Mapping blue-ice areas in Antarctica using ETM+ and MODIS data. Annals of Glaciology 55, 129–137. doi: 10.3189/2014aog66a069.

Hvidberg, C.S., Fishbaugh, K.E., Winstrup, M., Svensson, A., Byrne, S., Herkenhoff, K.E., 2012. Reading the climate record of the martian polar layered deposits. Icarus 221, 405–419. doi: 10.1016/j.icarus.2012.08.009.

Incropera, F.P., Lavine, A.S., Bergman, T.L., DeWitt, D.P., 2007. Fundamentals of heat and mass transfer. 6 ed., Wiley.

Ingersoll, 1970. Mars: Occurrence of Liquid Water. Science 168, 1–2. doi: 10.1126/science.168.3934.972.

Ingersoll, A.P., Summers, M.E., Schlipf, S.G., 1985. Supersonic Meteorology of Io: Sublimation-Driven Flow of SO2. Icarus 64, 375–390. doi: 10.1016/0019-1035(85)90062-4.

Ivanov, A.B., Muhleman, D.O., 2000. The Role of Sublimation for the Formation of the Northern Ice Cap: Results from the Mars Orbiter Laser Altimeter. Icarus 144, 436–448. doi: 10.1006/icar.1999.6304.

Jakosky, B.M., 1985. The seasonal cycle of water on Mars. Space Science Reviews 41, 131–200. doi: 10.1007/BF00241348.

James, P.B., 1982. The Seasonal CO2 Cycle on Mars: An Application of an Energy Balance Climate Model. Journal of Geophysical Research 87, 271–283. doi: 10.1029/JB087iB12p10271.

Jia, P., Andreotti, B., Claudin, P., 2017. Giant ripples on comet 67P/ChuryumovGerasimenko sculpted by sunset thermal wind. Proceedings of the National Academy of Sciences 114, 2509–2514. URL: http://www.pnas.org/lookup/doi/10.1073/pnas.1612176114, doi: 10.1073/pnas.1612176114.

Jiang, C., Douté, S., Luo, B., Zhang, L., 2017. Fusion of photogrammetric and photoclinometric information for high-resolution DEMs from Mars in-orbit imagery. ISPRS Journal of Photogrammetry and Remote Sensing 130, 418–430. URL: http://dx.doi.org/10.1016/j.isprsjprs.2017.06.010, doi: 10.1016/j.isprsjprs.2017.06.010.

Kahn, R.A., Lee, S.W., Martin, T.Z., Zurek, R.W., 1992. The Martian Dust Cycle, in: Mars. February, pp. 1017–1053. doi: 10.1016/j.cca.2006.01.021.

Kauhanen, J., Siili, T., Ja, S., Savija, H., 2008. The Mars limited area model and simulations of atmospheric circulations for the Phoenix landing area and season of operation. Journal of Geophysical Research 113. doi: 10.1029/2007JE003014.

Keller, H.U., Mottola, S., Davidsson, B., Schroder, S.E., Skorov, Y., Kuhrt, E., Groussin, O., Pajola, M., Hviid, S.F., Preusker, F., Scholten, F., A'Hearn, M.F., Sierks, H., Barbieri, C., Lamy, P., Rodrigo, R., Koschny, D., Rickman, H., Barucci, M.A., Bertaux, J.L., Bertini, I., Cremonese, G., Da Deppo, V., Debei, S., De Cecco, M., Fornasier, S., Fulle, M., Gutierrez, P.J., Ip, W.H., Jorda, L., Knollenberg, J., Kramm, J.R., Kuppers, M., Lara, L.M., Lazzarin, M., Lopez Moreno, J.J., Marzari, F., Michalik, H., Naletto, G., Sabau, L., Thomas, N., Vincent, J.B., Wenzel, K.P., Agarwal, J., Guttler, C., Oklay, N., Tubiana, C., 2015. Insolation, erosion, and morphology of comet 67P/Churyumov-Gerasimenko. Astronomy and Astrophysics 583. doi: 10.1051/0004-6361/201525964.

Kelly, N.J., Boynton, W.V., Kerry, K.E., Hamara, D., Janes, D.M., Reddy, R.C., Kim, K.J., Haberle, R.M., 2007. Seasonal polar carbon dioxide frost on Mars: CO2 mass and columnar thickness distribution. Journal of Geophysical Research E: Planets 112, 1–12. doi: 10.1029/2006JE002678.

Khayat, A.S., Smith, M.D., Guzewich, S.D., 2019. Understanding the water cycle above the north polar cap on Mars using MRO CRISM retrievals of water vapor. Icarus 321, 722–735. URL: doi:10.1016/j.icarus.2018.12.024, doi: 10.1016/j.icarus.2018.12.024.

Kieffer, H.H., Chase, S.C., Martin, T.Z., Miner, E.D., Palluconi, F.D., 1976. Martian North Pole Summer Temperatures: Dirty Water Ice. Science (New York, N.Y.) 194, 1341–1344. URL:

http://www.sciencemag.org/content/194/4271/1341.abstract, doi: 10.1126/science.194.4271.1341.

Kimura, J., Kawamura, T., Morito, H., Morota, T., Honda, C., Kuramoto, K., Okada, T., 2011. Sublimation's impact on temporal change of albedo dichotomy on Iapetus. Icarus 214, 596–605. URL: http://dx.doi.org/10.1016/j.icarus.2011.06.015, doi: 10.1016/j.icarus.2011.06.015.

Kok, J.F., Parteli, E.J., Michaels, T.I., Karam, D.B., 2012. The physics of wind-blown sand and dust. Reports on Progress in Physics 75. doi: 10.1088/0034-4885/75/10/106901.

Kuzan, J., Hanratty, T., Adrian, R., 1989. Turbulent flows with incipient separation over solid waves. Experiments in Fluids 7. URL: http://link.springer.com/10.1007/BF00207300, doi: 10.1007/BF00207300.

Lancaster, N., 1995. Geomorphology of Desert Dunes. Routledge, London.

Lapotre, M.G., Ewing, R.C., Lamb, M.P., Fischer, W.W., Grotzinger, J.P., Rubin, D.M., Lewis, K.W., Ballard, M.J., Day, M., Gupta, S., Banham, S.G., Bridges, N.T., Marais, D.J., Fraeman, A.A., Grant, J.A., Herkenhoff, K.E., Ming, D.W., Mischna, M.A., Rice, M.S., Sumner, D.A., Vasavada, A.R., Yingst, R.A., 2016. Large wind ripples on Mars: A record of atmospheric evolution. Science 353, 55–58. doi: 10.1126/science.aaf3206.

Lapotre, M.G., Ewing, R.C., Weitz, C.M., Lewis, K.W., Lamb, M.P., Ehlmann, B.L., Rubin, D.M., 2018. Morphologic Diversity of Martian Ripples: Implications for Large-Ripple Formation. Geophysical Research Letters 45, 10,229–10,239. doi: 10.1029/2018GL079029.

Law, J., Van Dijk, D., 1994. Sublimation as a Geomorphic Process: A review. Permafrost and Periglacial Processes 5, 237–249. doi: 10.1002/ppp.3430050404.

Lebofsky, L., 1977. Identification of water frost on Callisto. Nature 269, 785–787. doi: 10.1038/269785a0.

Lee, P., Thomas, P.C., 1995. Longitudinal dunes on Mars: relation to current wind regimes. Journal of Geophysical Research 100, 5381–5395. doi: 10.1029/95JE00225.

Livingstone, I., Warren, A., 2019. Aeolian Geomorphology: A New Introduction. Wiley. URL: https://books.google.fr/books?id=2paADwAAQBAJ.

Lorenz, R.D., Radebaugh, J., 2009. Global pattern of Titan's dunes: Radar survey from the Cassini prime mission. Geophysical Research Letters 36, 11–14. doi: 10.1029/2008GL036850.

Lorenz, R.D., Zimbelman, J.R., 2014. Dune Worlds: How Windblown Sand Shapes Planetary

Landscapes. Springer-Verlag Berlin Heidelberg. URL: https://books.google.fr/books?id=-AO7BAAAQBAJ.

Loyd, R.J., Moffat, R.J., Kays, W.M., 1970. The Turbulent Boundary Layer on a Porous Plate: an Experimental Study of the Fluid Dynamics with Strong Favorable Pressure Gradients and Blowing. Department of Mechanical Engineering, Stanford University. URL: https://books.google.fr/books?id=cTYEAAAAIAAJ.

Malin, M.C., Edgett, K.S., 2001. Mars Global Surveyor Mars Orbiter Camera: Interplanetary cruise through primary mission. Journal of Geophysical Research 106, 23,429–23,570. doi: 10.1029/2000JE001455.

Mangold, N., 2011. Ice sublimation as a geomorphic process: A planetary perspective. Geomorphology 126, 1–17. URL: http://dx.doi.org/10.1016/j.geomorph.2010.11.009, doi: 10.1016/j.geomorph.2010.11.009.

Marshall, P., Brown, M.C., 1974. Ice in Coulthard Cave, Alberta. Canadian Journal of Earth Sciences 11, 510–518. doi: 10.1139/e74-045.

Massé, M., Bourgeois, O., Mouélic, S.L., Verpoorter, C., Spiga, A., Deit, L.L., 2012. Wide distribution and glacial origin of polar gypsum on Mars. Earth and Planetary Science Letters 317-318, 44–55. URL: http://dx.doi.org/10.1016/j.epsl.2011.11.035, doi: 10.1016/j.epsl.2011.11.035.

May, B., Spötl, C., Wagenbach, D., Dublyansky, Y., Liebl, J., 2011. First investigations of an ice core from Eisriesenwelt cave (Austria). Cryosphere 5, 81–93. doi: 10.5194/tc-5-81-2011.

Meakin, P., Jamtveit, B., 2010. Geological pattern formation by growth and dissolution in aqueous systems. Proceedings of the Royal Society A: Mathematical, Physical and Engineering Sciences 466, 659–694. URL: http://rspa.royalsocietypublishing.org/cgi/doi/10.1098/rspa.2009.0189, doi: 10.1098/rspa.2009.0189.

Mellor, M., Swithinbank, C., 1989. Airfields on Antarctic glacier ice. Technical Report. Cold Region Research and Engineering Lab. Hanover NH.

Millour, E., Forget, F., Spiga, A., Vals, M., Zakharov, V., Montabone, L., Montmessin, F., Read, P.L., Cipriani, F., 2018. The Mars Climate Database (Version 5.3), in: Scientific Workshop: From Mars Express to ExoMars, ESAC Madrid. pp. 27–28.

Moore, J.M., Howard, A.D., Umurhan, O.M., White, O.L., Schenk, P.M., Beyer, R.A., McKinnon,

W.B., Spencer, J.R., Singer, K.N., Grundy, W.M., Earle, A.M., Schmitt, B., Protopapa, S., Nimmo, F., Cruikshank, D.P., Hinson, D.P., Young, L.A., Stern, S.A., Weaver, H.A., Olkin, C.B., Ennico, K., Collins, G., Bertrand, T., Forget, F., Scipioni, F., 2018. Bladed Terrain on Pluto: Possible origins and evolution. Icarus 300, 129–144. doi: 10.1016/j.icarus.2017.08.031.

Murray, B.C., Soderblom, L.A., Cutts, J.A., Sharp, R.P., Milton, D.J., 1972. Geological Framework of the South Polar Region of Mars. Icarus 17, 328–345. doi: 10.1016/0019-1035(72)90004-8.

Nathues, A., Hoffmann, M., Schaefer, M., Le Corre, L., Reddy, V., Platz, T., Cloutis, E.A., Christensen, U., Kneissl, T., Li, J.Y., Others, 2015. Sublimation in bright spots on (1) Ceres. Nature 528, 237.

Ng, F.S., Zuber, M.T., 2006. Patterning instability of a growing polar ice cap. Journal of Geophysical Research E: Planets 111, 1–14. doi: 10.1029/2005JE002533.

Nguyen, T.G., Radebaugh, J., Innanen, A., Moores, J.E., 2020. A survey of small-scale surface features on the Martian north polar cap using HiRISE. Planetary and Space Science 182, 104809. URL: doi:10.1016/j.pss.2019.104809, doi: 10.1016/j.pss.2019.104809.

Obleitner, F., Spötl, C., 2011. The mass and energy balance of ice within the Eisriesenwelt cave, Austria. Cryosphere 5, 245–257. doi: 10.5194/tc-5-245-2011.

Pankine, A.A., Tamppari, L.K., 2015. Constraints on water vapor vertical distribution at the Phoenix landing site during summer from MGS TES day and night observations. Icarus 252, 107–120. URL: http://dx.doi.org/10.1016/j.icarus.2015.01.008, doi: 10.1016/j.icarus.2015.01.008.

Pankine, A.A., Tamppari, L.K., Smith, M.D., 2010. MGS TES observations of the water vapor above the seasonal and perennial ice caps during northern spring and summer. Icarus 210, 58–71. URL: http://dx.doi.org/10.1016/j.icarus.2010.06.043, doi: 10.1016/j.icarus.2010.06.043.

Peroiu, A., Onac, B.P., Peroiu, I., 2011. The interplay between air temperature and ice mass balance changes in Scrioara Ice Cave, Romania. Acta Carsologica 40, 445–456. doi: 10.3986/ac.v40i3.4.

Persoiu, A., Lauritzen, S.E., 2018. Ice caves. Elsevier Science.

Petrosyan, A., Galperin, B., Larsen, S.E., Lewis, S., Maattanen, A., Read, P.L., Renno, N., Rogberg, L., Savijarvi, H., Siili, T., Spiga, A., Toigo, A., Vazquez, L., 2011. The Martian

atmospheric boundary layer. Reviews of Geophysics 49. doi: 10.1029/2010RG000351.

Protopapa, S., Grundy, W.M., Reuter, D.C., Hamilton, D.P., Dalle Ore, C.M., Cook, J.C., Cruikshank, D.P., Schmitt, B., Philippe, S., Quirico, E., Binzel, R.P., Earle, A.M., Ennico, K., Howett, C.J., Lunsford, A.W., Olkin, C.B., Parker, A., Singer, K.N., Stern, A., Verbiscer, A.J., Weaver, H.A., Young, L.A., 2017. Pluto's global surface composition through pixel-by-pixel Hapke modeling of New Horizons Ralph/LEISA data. Icarus 287, 218–228. URL: http://dx.doi.org/10.1016/j.icarus.2016.11.028, doi: 10.1016/j.icarus.2016.11.028.

Rodriguez, S., Le Mouélic, S., Barnes, J.W., Kok, J.F., Rafkin, S.C.R., Lorenz, R.D., Charnay, B., Radebaugh, J., Narteau, C., Cornet, T., Bourgeois, O., Lucas, A., Rannou, P., Griffith, C.A., Coustenis, A., Appéré, T., Hirtzig, M., Sotin, C., Soderblom, J.M., Brown, R.H., Bow, J., Vixie, G., Maltagliati, L., Courrech du Pont, S., Jaumann, R., Stephan, K., Baines, K.H., Buratti, B.J., Clark, R.N., Nicholson, P.D., 2018. Observational evidence for active dust storms on Titan at equinox. Nature Geoscience 11, 727–232. URL: http://www.nature.com/articles/s41561-018-0233-2, doi: 10.1038/s41561-018-0233-2.

Schaefer, L., Jr, B.F., 2004. Heavy metal frost on Venus. Icarus 168, 215–219. doi: 10.1016/j.icarus.2003.11.023.

Schmidt, R.A., 1980. Threshold windspeeds and elastic impact in snow transport. Journal of Glaciology 26, 453–467. doi: 10.1017/S0022143000010972.

Short, M.B., Baygents, J.C., Beck, J.W., Stone, D.A., Toomey, R.S., Goldstein, R.E., 2005. Stalactite Growth as a Free-Boundary Problem: A Geometric Law and Its Platonic Ideal. Physical Review Letters 94, 14–17. doi: 10.1103/PhysRevLett.94.018501.

Skorov, Y.V., Markiewicz, W.J., Basilevsky, A.T., Keller, H.U., 2001. Stability of water ice under a porous nonvolatile layer: Implications to the south polar layered deposits of Mars. Planetary and Space Science 49, 59–63. doi: 10.1016/S0032-0633(00)00121-5.

Smith, I.B., Holt, J.W., 2010. Onset and migration of spiral troughs on Mars revealed by orbital radar. Nature 465, 450–453. URL: http://dx.doi.org/10.1038/nature09049, doi: 10.1038/nature09049.

Smith, I.B., Holt, J.W., 2015. Spiral Trough Diversity on the North Pole of Mars, as seen by Shallow Radar (SHARAD). Journal of Geophysical Research: Planets 120, 362–387. doi: 10.1002/2014JE004720.

Smith, I.B., Holt, J.W., Spiga, A., Howard, A.D., Parker, G., 2013. The Spiral troughs of Mars as

cyclic steps. Journal of Geophysical Research: Planets 118, 1835–1857. doi: 10.1002/jgre.20142.

Smith, I.B., Spiga, A., 2018. Seasonal variability in winds in the north polar region of Mars. Icarus 308, 188–196. URL: doi:10.1016/j.icarus.2017.10.005, doi: 10.1016/j.icarus.2017.10.005.

Squyres, S.W., 1980. Surface temperatures and retention of H2O frost on Ganymede and Callisto. Icarus 44, 502–510. doi: 10.1016/0019-1035(80)90040-8.

Sunshine, J.M., Thomas, N., El-Maarry, M.R., Farnham, T.L., 2016. Evidence for geologic processes on comets. Journal of Geophysical Research: Planets 121, 2194–2210. doi: 10.1002/2016JE005119.

Swain, M., Gallée, H., 2006. Antarctic Boundary Layer Seeing. Publications of the Astronomical Society of the Pacific 118, 1190–1197. doi: 10.1086/507153.

Telfer, M.W., Parteli, E.J.R., Radebaugh, J., Beyer, R.A., Bertrand, T., Forget, F., Nimmo, F., Grundy, W.M., Moore, J.M., Stern, S.A., Spencer, J., Lauer, T.R., Earle, A.M., Binzel, R.P., Weaver, H.A., Olkin, C.B., Young, L.A., Ennico, K., Runyon, K., The New Horizons Geology, G., Team, I.S.T., 2018. Dunes on Pluto. Science 360, 992–997. URL: http://science.sciencemag.org/content/360/6392/992?utm_campaign=toc_sci-mag_2018-05-31&et_rid=71603393&et_cid=2086538, doi: 10.1126/SCIENCE.AAO2975.

Thomas, N., Davidsson, B., El-Maarry, M.R., Fornasier, S., Giacomini, L., Gracia-Berná, A.G., Hviid, S.F., Ip, W.H., Jorda, L., Keller, H.U., Knollenberg, J., Kührt, E., La Forgia, F., Lai, I.L., Liao, Y., Marschall, R., Massironi, M., Mottola, S., Pajola, M., Poch, O., Pommerol, A., Preusker, F., Scholten, F., Su, C.C., Wu, J.S., Vincent, J.B., Sierks, H., Barbieri, C., Lamy, P.L., Rodrigo, R., Koschny, D., Rickman, H., A'Hearn, M.F., Barucci, M.A., Bertaux, J.L., Bertini, I., Cremonese, G., Da Deppo, V., Debei, S., De Cecco, M., Fulle, M., Groussin, O., Gutierrez, P.J., Kramm, J.R., Küppers, M., Lara, L.M., Lazzarin, M., Lopez Moreno, J.J., Marzari, F., Michalik, H., Naletto, G., Agarwal, J., Güttler, C., Oklay, N., Tubiana, C., 2015. Redistribution of particles across the nucleus of comet 67P/Churyumov-Gerasimenko. Astronomy and Astrophysics 583, 1–18. doi: 10.1051/0004-6361/201526049.

Thomas, R., 1979. Size of scallops and ripples formed by flowing water. Nature 277, 281—-283.

Thorness, C.B., Hanratty, T.J., 1979. Mass transfer between a flowing fluid and a solid wavy surface. AIChE Journal 25, 686–697. URL: http://onlinelibrary.wiley.com/doi/10.1002/aic.690250415/abstract, doi:

10.1002/aic.690250415.

Tokano, T., 2008. Dune-forming winds on Titan and the influence of topography. Icarus 194, 243–262. doi: 10.1016/j.icarus.2007.10.007.

Tokano, T., 2010. Relevance of fast westerlies at equinox for the eastward elongation of Titan's dunes. Aeolian Research 2, 113–127. URL: http://dx.doi.org/10.1016/j.aeolia.2010.04.003, doi: 10.1016/j.aeolia.2010.04.003.

Ueno, K., 2007. Characteristics of the wavelength of ripples on icicles. Physics of Fluids 19. doi: 10.1063/1.2775484.

Ueno, K., Farzaneh, M., Yamaguchi, S., Tsuji, H., 2010. Numerical and experimental verification of a theoretical model of ripple formation in ice growth under supercooled water film flow. Fluid Dynamics Research 42. doi: 10.1088/0169-5983/42/2/025508.

Warner, N.H., Farmer, J.D., 2008. Importance of aeolian processes in the origin of the north polar chasmata, Mars. Icarus 196, 368–384. doi: 10.1016/j.icarus.2007.08.043.

Weller, G., 1969. The heat and mass balance of snow dunes on the central Antarctic plateau. Journal of Glaciology 8, 277–284. URL: http://adsabs.harvard.edu/abs/1969JGlac...8..277W, doi: 10.3189/S0022143000031257.

White, O.L., Moore, J.M., McKinnon, W.B., Spencer, J.R., Howard, A.D., Schenk, P.M., Beyer, R.A., Nimmo, F., Singer, K.N., Umurhan, O.M., Stern, S.A., Ennico, K., Olkin, C.B., Weaver, H.A., Young, L.A., Cheng, A.F., Bertrand, T., Binzel, R.P., Earle, A.M., Grundy, W.M., Lauer, T.R., Protopapa, S., Robbins, S.J., Schmitt, B., 2017. Geological mapping of Sputnik Planitia on Pluto. Icarus 287, 261–286. URL: http://dx.doi.org/10.1016/j.icarus.2017.01.011, doi: 10.1016/j.icarus.2017.01.011.

Winkler, M., Juen, I., Mölg, T., Wagnon, P., Gómez, J., Kaser, G., Winkler, M., Juen, I., Mölg, T., Wagnon, P., Gómez, J., 2009. Measured and modelled sublimation on the tropical Glaciar Artesonraju, Perú. The Cryosphere 3, 21–30. doi: 10.5194/tc-3-21-2009.

Winther, J.G., Jespersen, M.N., Liston, G.E., 2001. Blue-ice areas in Antarctica derived from NOAA AVHRR satellite data. Journal of Glaciology 47, 325–334. doi: 10.3189/172756501781832386.

Declaration of interests

☒ The authors declare that they have no known competing financial interests or personal relationships that could have appeared to influence the work reported in this paper.

☐The authors declare the following financial interests/personal relationships which may be considered as potential competing interests:

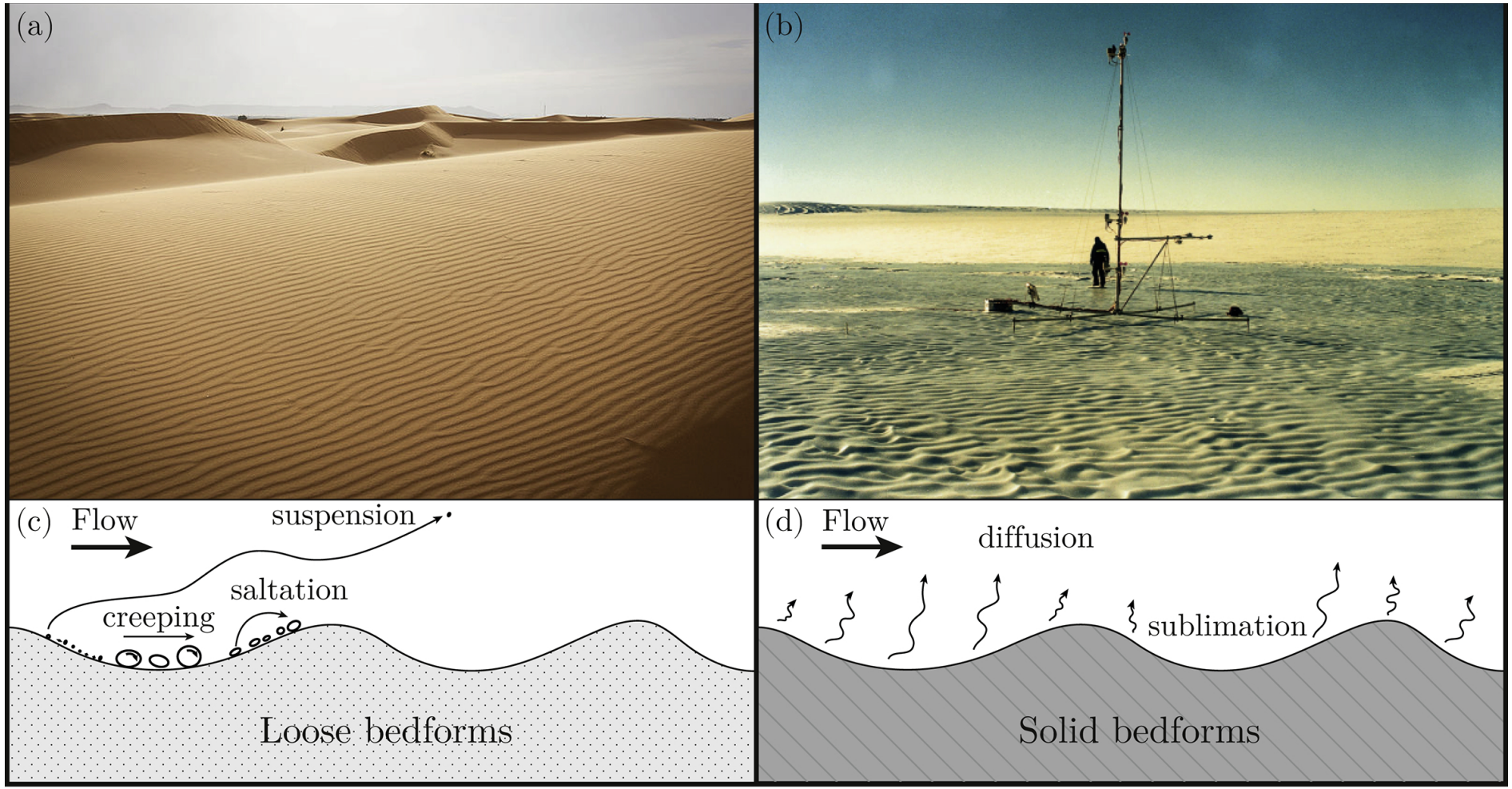
(a)
(b)
(c) Flow
suspension
saltation
creeping
Loose bedforms
(d) Flow
diffusion
sublimation
Solid bedforms

Figure 1

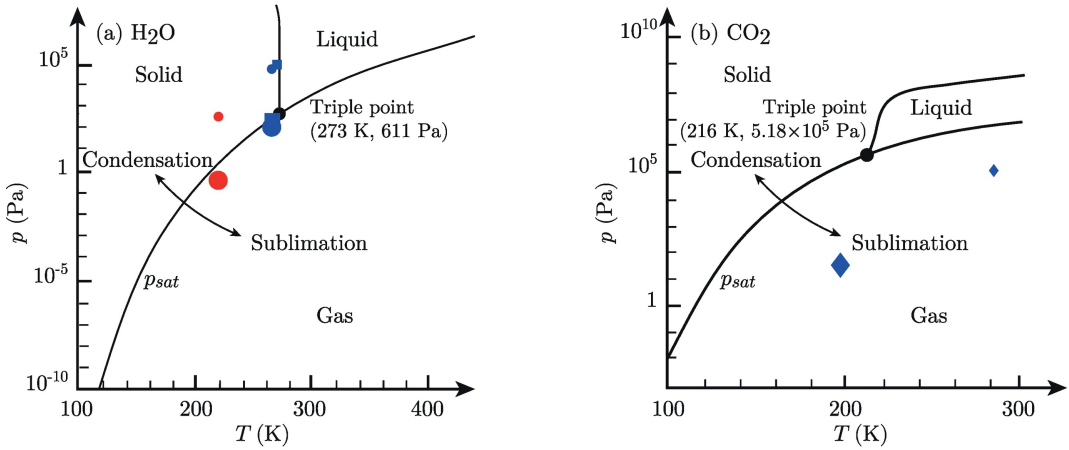
(a) H2O
Solid
Liquid
Triple point
(273 K, 611 Pa)
Condensation
Sublimation
psat
Gas
p (Pa)
T (K)
(b) CO2
Solid
Triple point
(216 K, 5.18×10^5 Pa)
Liquid
Condensation
Sublimation
psat
Gas
p (Pa)
T (K)
Ice cave (Eisriesenwelt)
Blue Ice Areas (Svea)
Experimental model
Martian North Polar Cap (MNPC)
pv, Tint
p, T

Figure 2

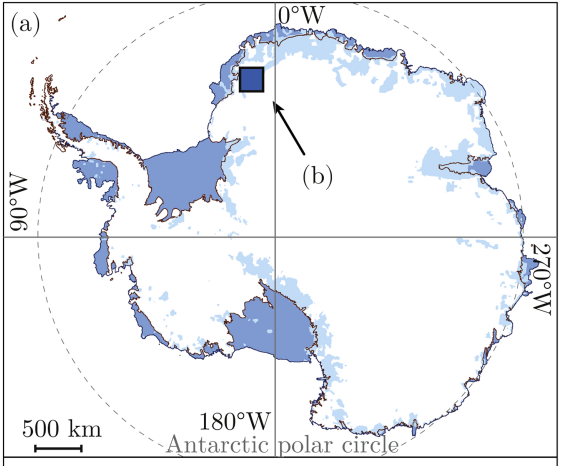
(a)
0°W
90°W
270°W
180°W
(b)
500 km
Antarctic polar circle
Coastline
Groundline
Ice Shelves
BIAs

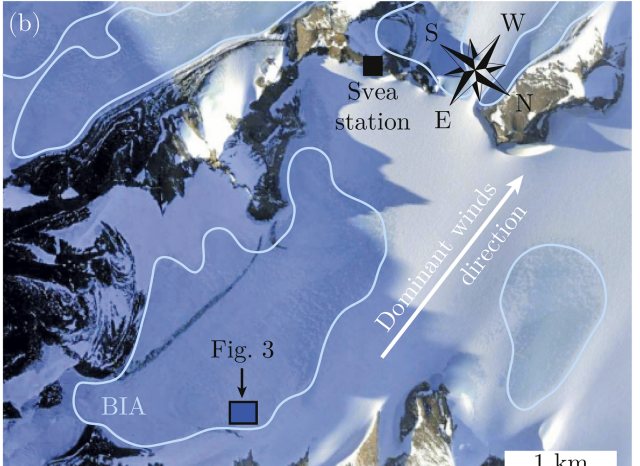
(b)
S
W
E
N
Svea
station
Dominant winds
direction
Fig. 3
BIA
1 km

Figure 3

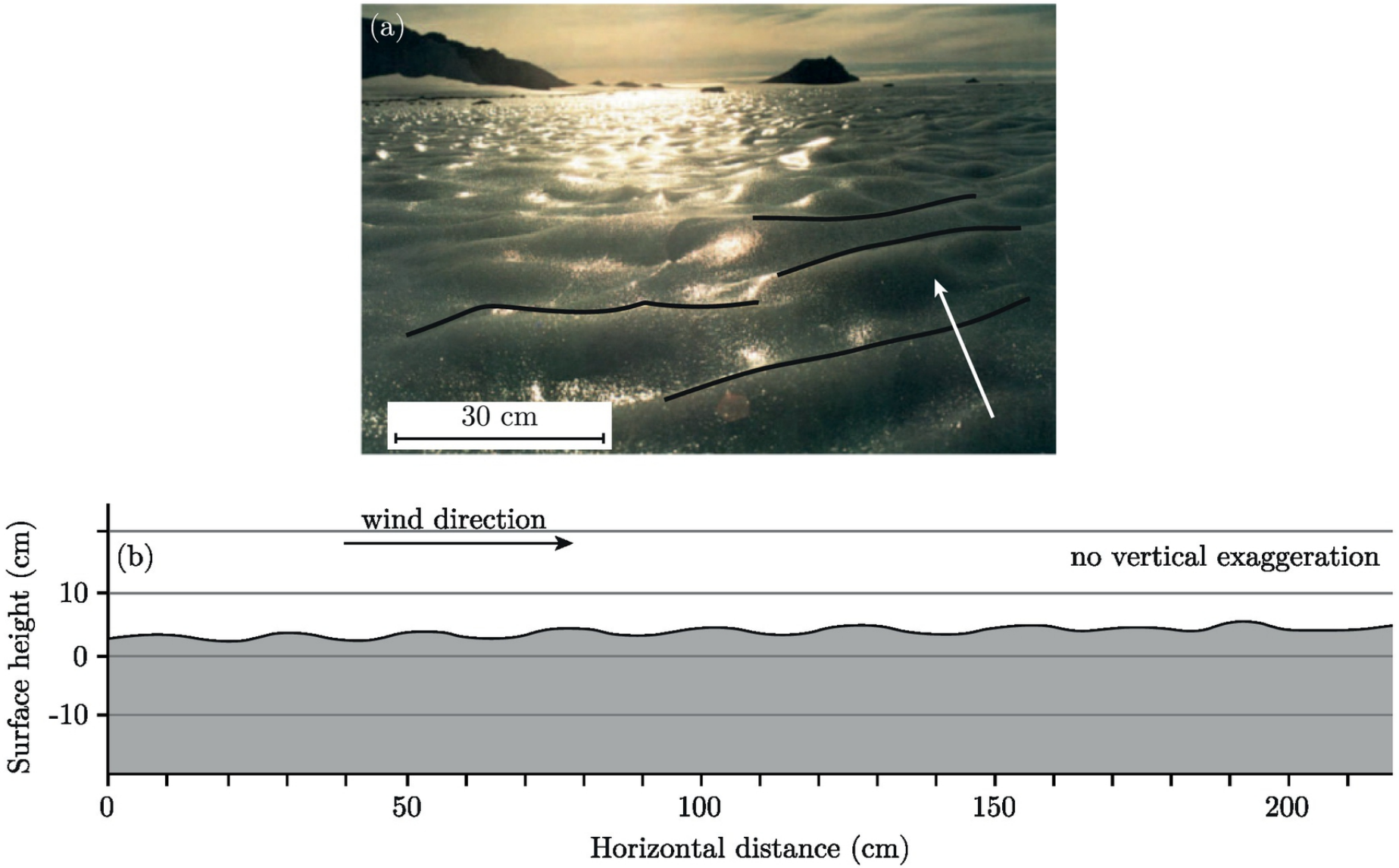
(a)
30 cm
wind direction
(b)
no vertical exaggeration
Surface height (cm)
10
0
-10
0
50
100
150
200
Horizontal distance (cm)

Figure 4

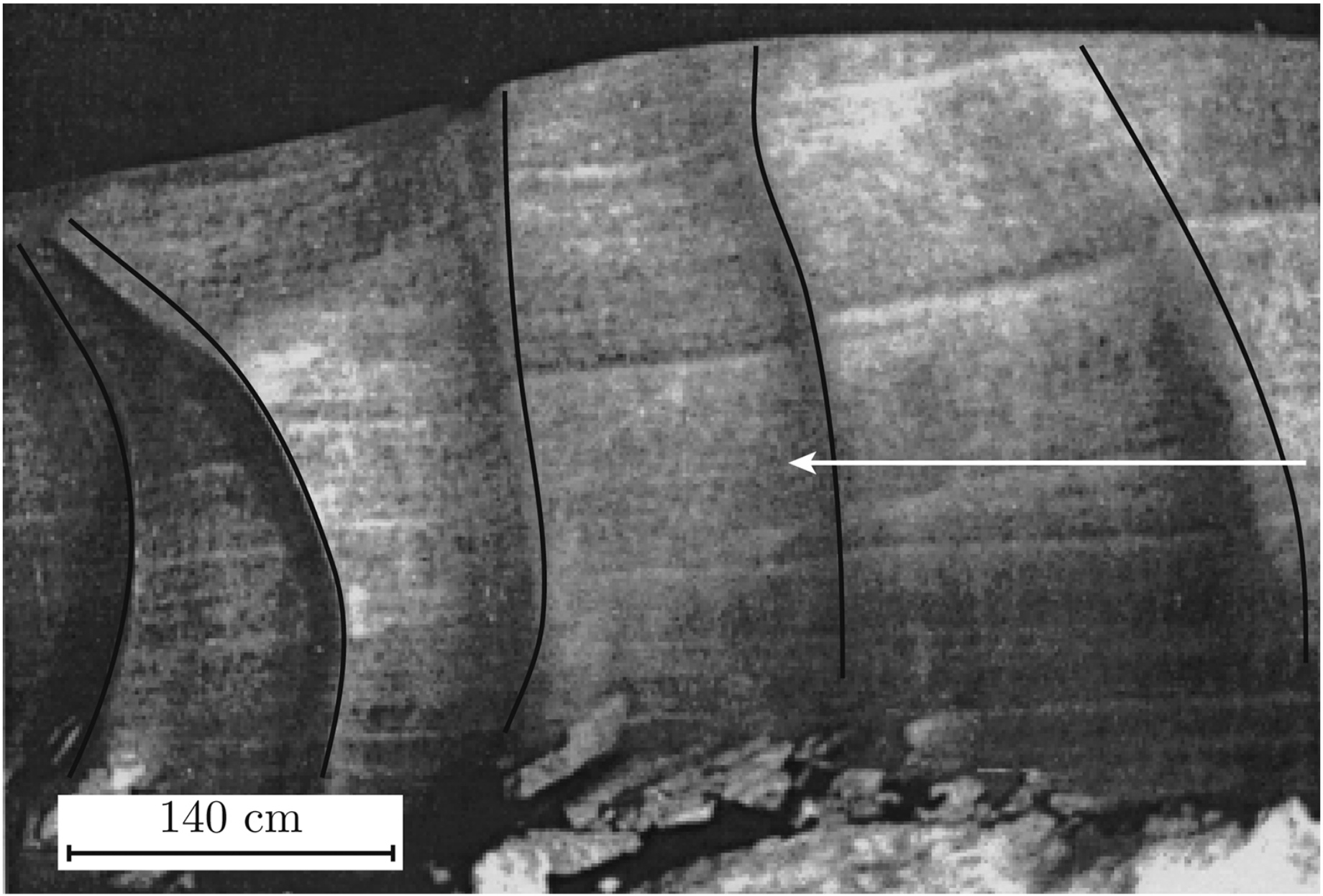

Figure 5

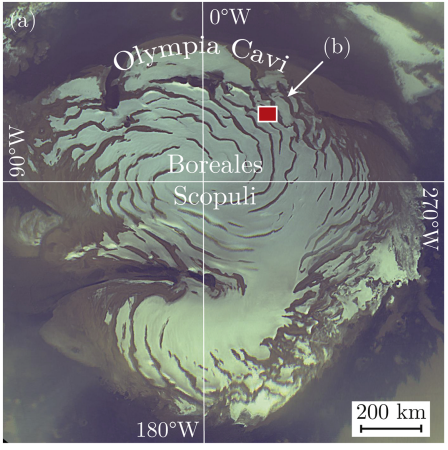
(a)
0°W
Olympia Cavi
(b)
90°W
Boreales
Scopuli
270°W
180°W
200 km

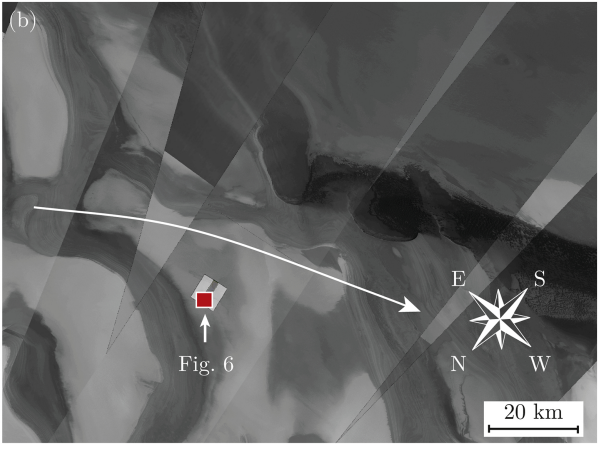
(b)
Fig. 6
E
S
N
W
20 km

Figure 6

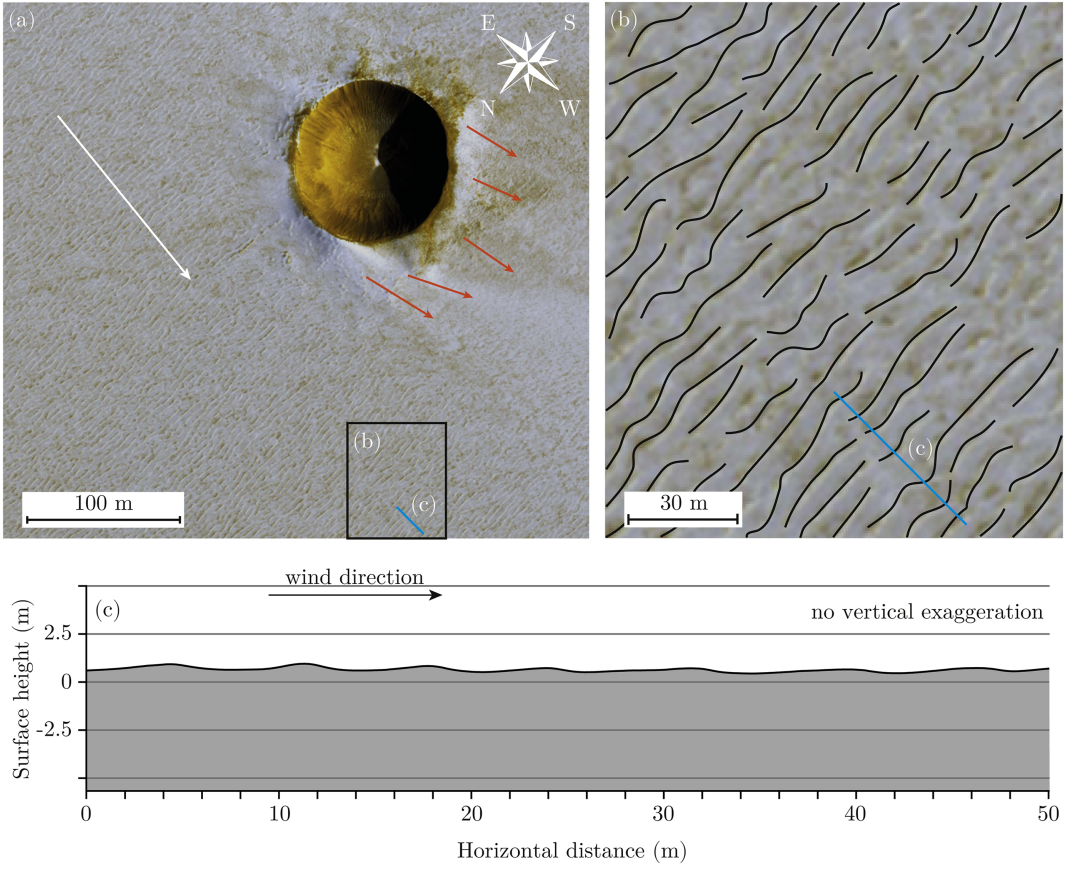
(a)
E
S
N
W
(b)
(c)
100 m
(b)
30 m
(c)
wind direction
(c)
no vertical exaggeration
Surface height (m)
2.5
0
-2.5
0
10
20
30
40
50
Horizontal distance (m)

Figure 7

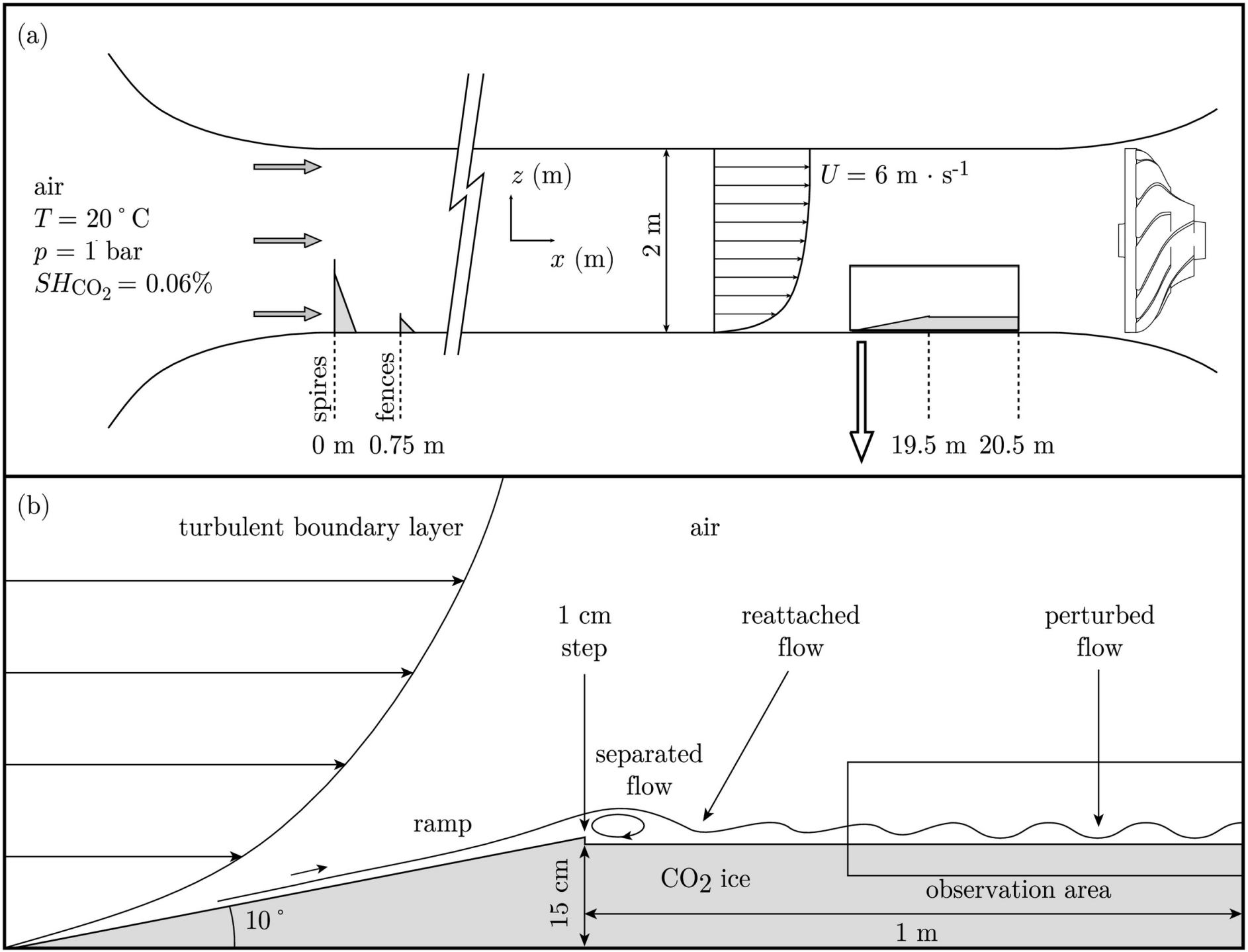
(a)
air
$T = 20\,^{\circ}\mathrm{C}$
$p = 1$ bar
$SH_{CO_2} = 0.06\%$
spires
fences
0 m
0.75 m
z (m)
x (m)
2 m
$U = 6\ \mathrm{m \cdot s^{-1}}$
19.5 m
20.5 m
(b)
turbulent boundary layer
air
1 cm step
reattached flow
perturbed flow
separated flow
ramp
CO_2 ice
observation area
15 cm
10 °
1 m

Figure 8

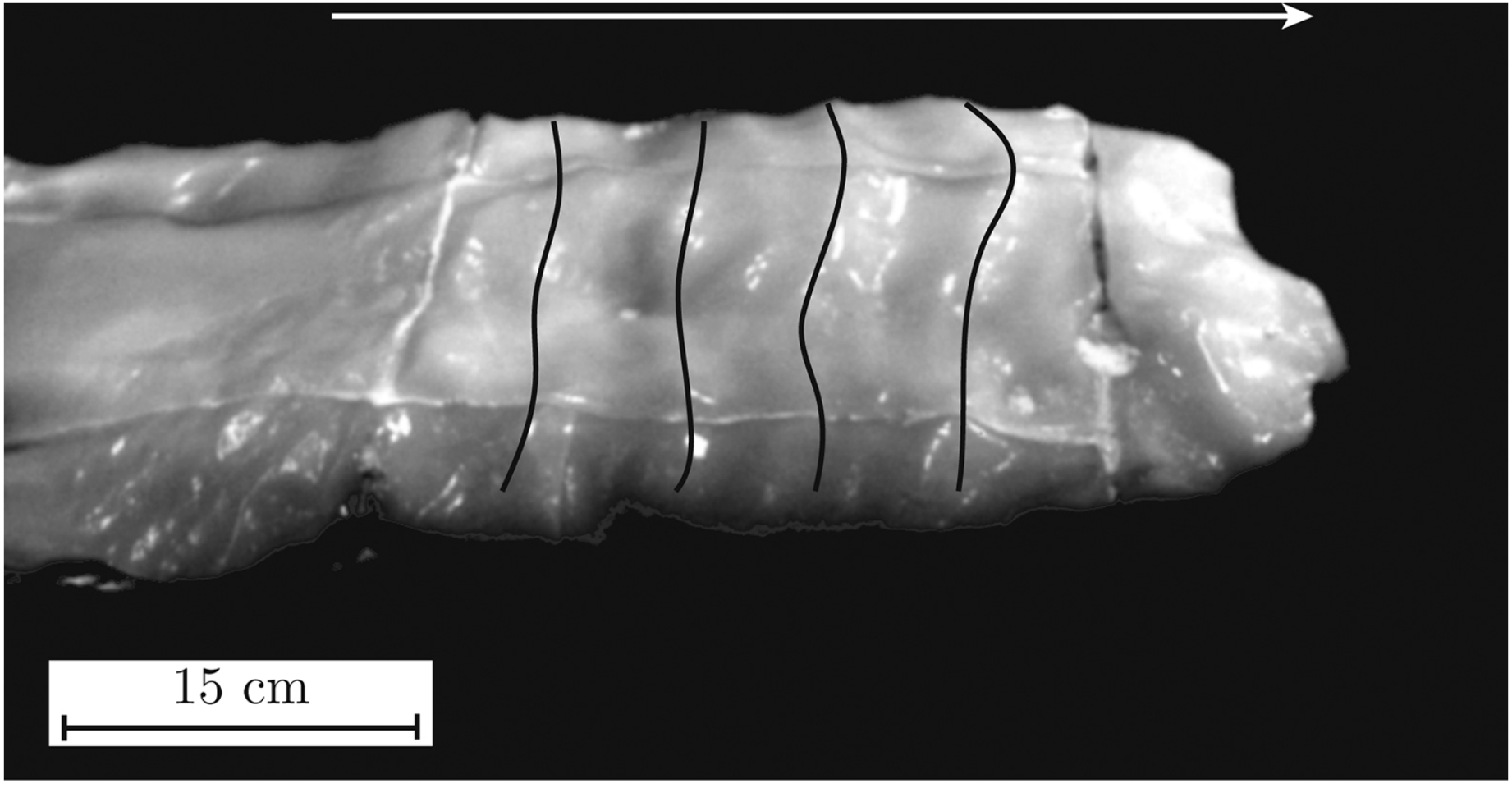

Figure 9

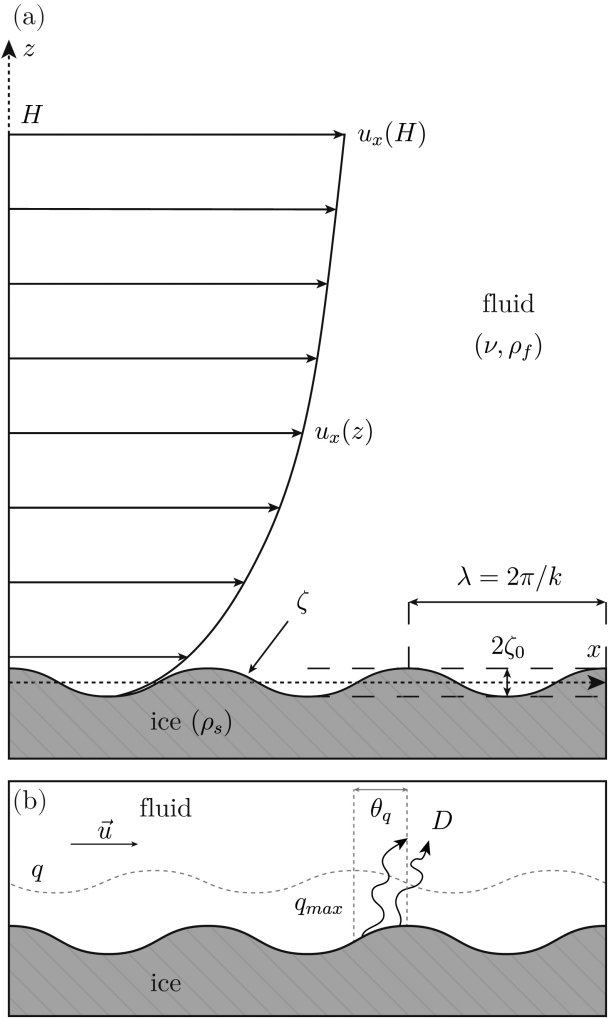
(a)
z
H
$u_x(H)$
fluid
(ν, ρ_f)
$u_x(z)$
$\lambda = 2\pi/k$
ζ
$2\zeta_0$
x
ice (ρ_s)
(b)
fluid
$\vec{u}$
θ_q
D
q
q_{max}
ice

Figure 10

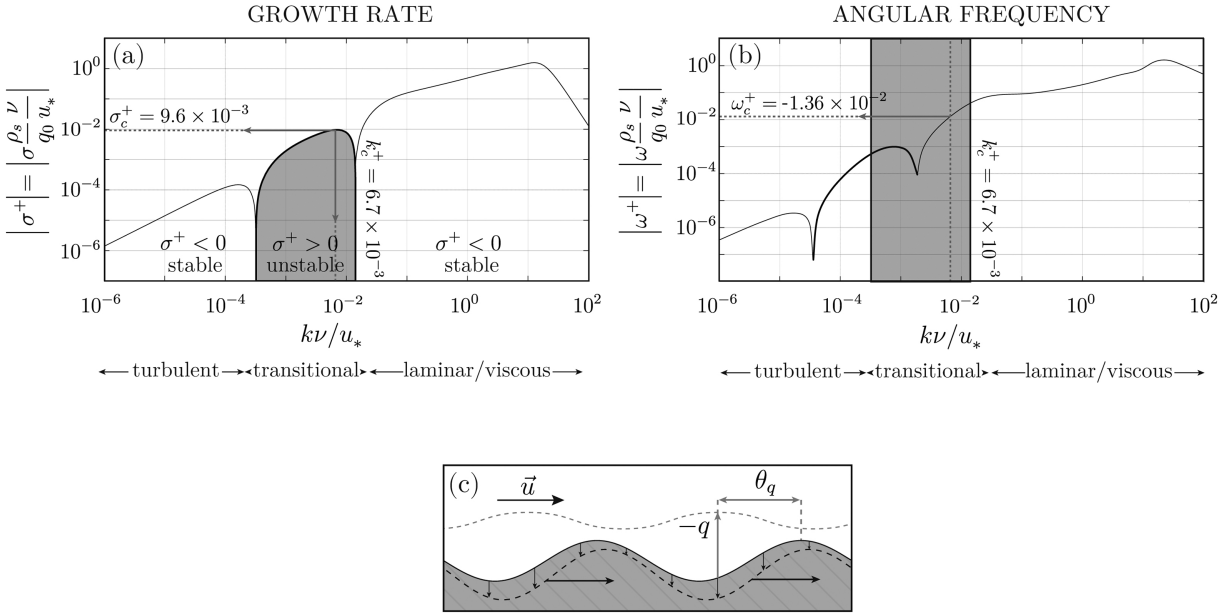
GROWTH RATE
ANGULAR FREQUENCY
(a)
(b)
(c)
$\sigma_c^+ = 9.6 \times 10^{-3}$
$\omega_c^+ = -1.36 \times 10^{-2}$
$k_c^+ = 6.7 \times 10^{-3}$
$\sigma^+ < 0$ stable
$\sigma^+ > 0$ unstable
$\sigma^+ < 0$ stable
$\left|\sigma^+\right| = \left|\sigma \frac{\rho_s}{\rho_0} \frac{\nu}{u_*}\right|$
$\left|\omega^+\right| = \left|\omega \frac{\rho_s}{\rho_0} \frac{\nu}{u_*}\right|$
$k\nu/u_*$
turbulent
transitional
laminar/viscous
$\vec{u}$
θ_q
$-q$

Figure 11

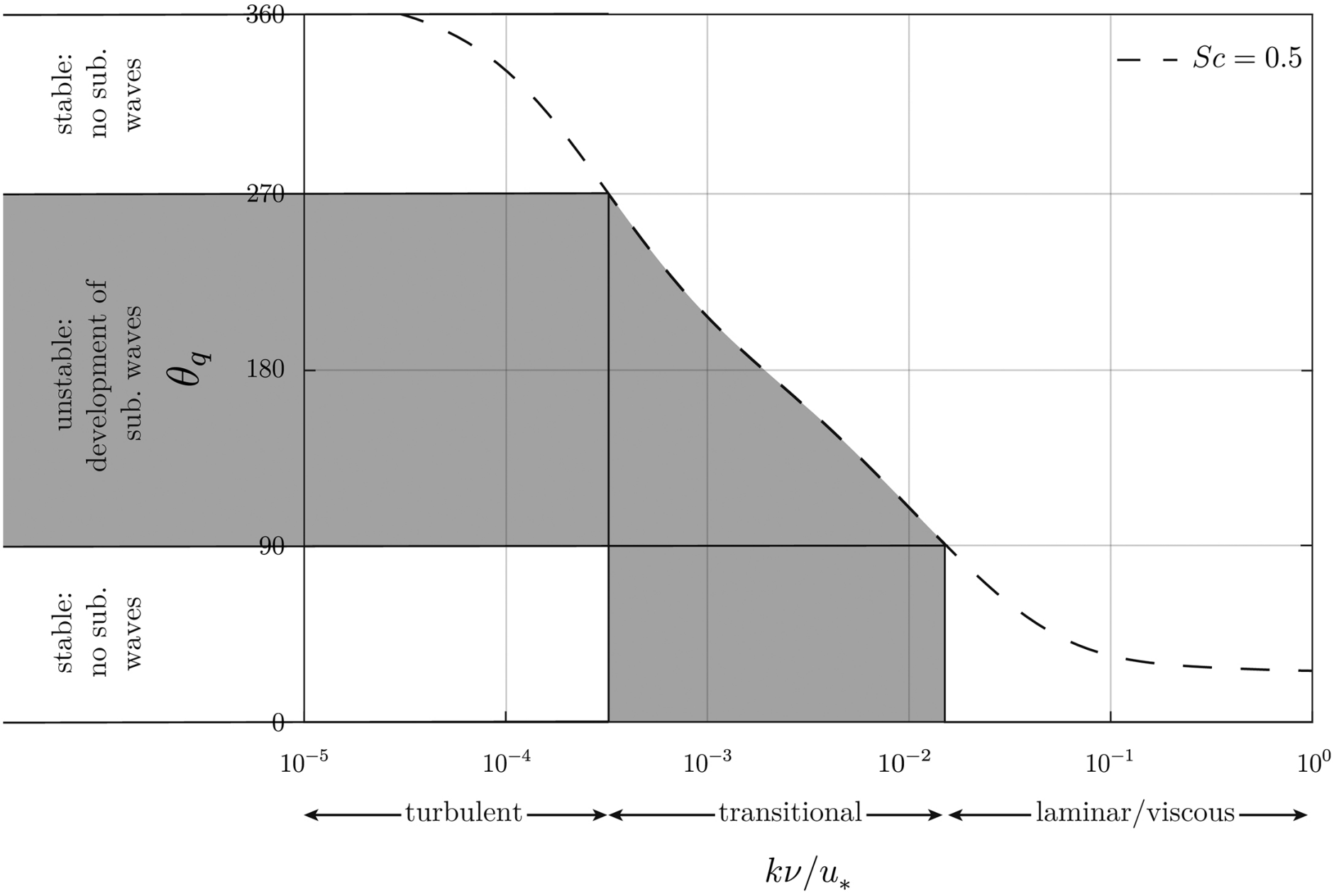
360
270
180
90
0
stable: no sub. waves
unstable: development of sub. waves
θ_q
stable: no sub. waves
$Sc = 0.5$
10^{-5}
10^{-4}
10^{-3}
10^{-2}
10^{-1}
10^{0}
turbulent
transitional
laminar/viscous
$k\nu/u_*$

Figure 12

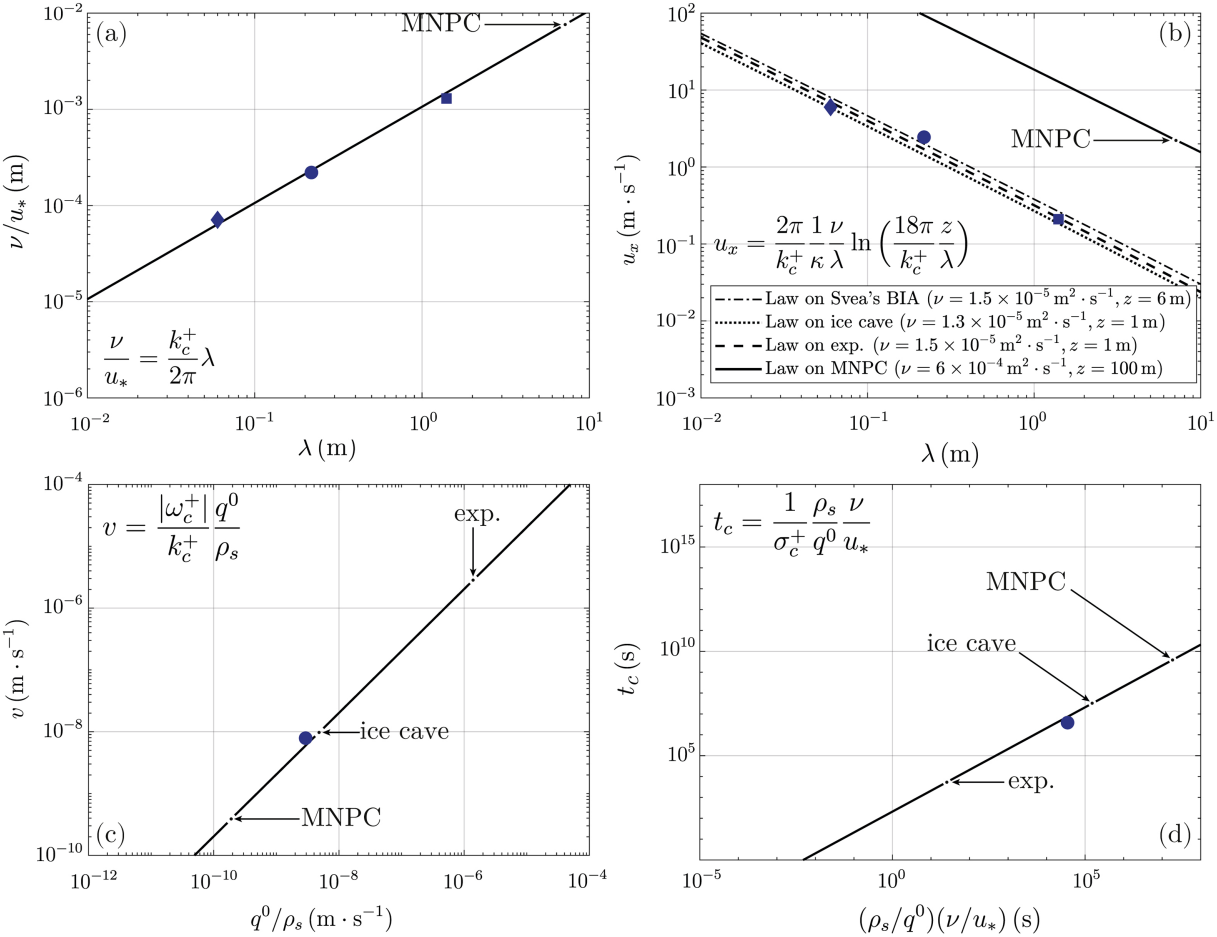

Model

– scaling laws from this work

Measurements

- Eisriesenwelt ice cave [45]
- ♦ experimental model
- Svea's BIA [47]

Figure 13

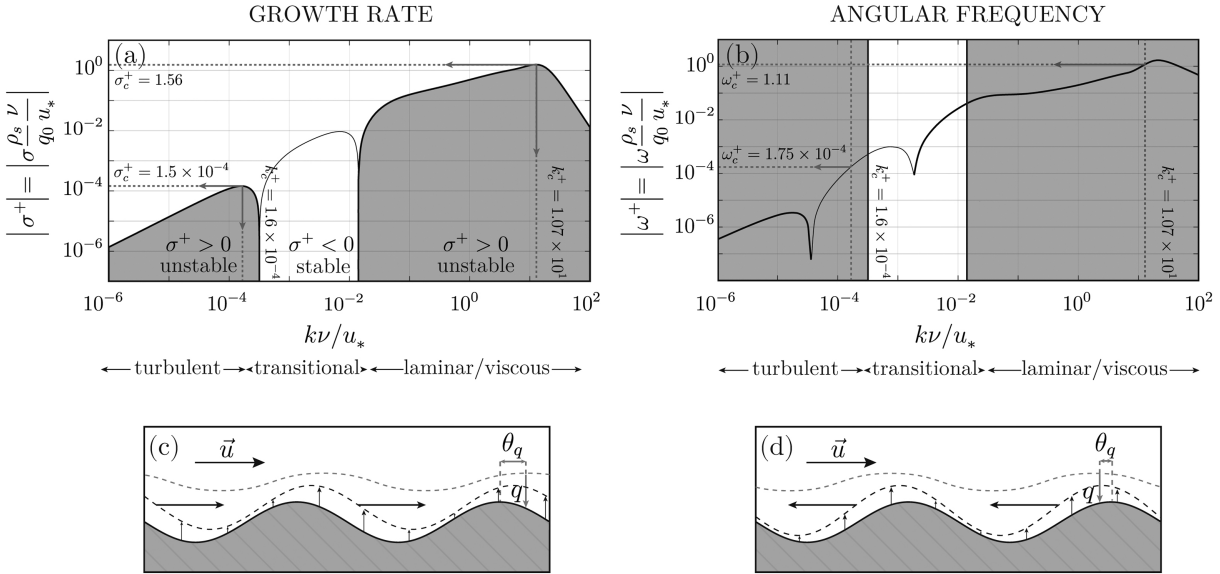
GROWTH RATE
ANGULAR FREQUENCY
(a)
(b)
(c)
(d)
$\sigma_c^+ = 1.56$
$\sigma_c^+ = 1.5 \times 10^{-4}$
$k_c^+ = 1.6 \times 10^{-4}$
$k_c^+ = 1.07 \times 10^1$
$\omega_c^+ = 1.11$
$\omega_c^+ = 1.75 \times 10^{-4}$
$\sigma^+ > 0$ unstable
$\sigma^+ < 0$ stable
$\sigma^+ > 0$ unstable
$|\sigma^+| = |\sigma \frac{\rho_s}{q_0} \frac{\nu}{u_*}|$
$|\omega^+| = |\omega \frac{\rho_s}{q_0} \frac{\nu}{u_*}|$
$k\nu/u_*$
turbulent
transitional
laminar/viscous
$\vec{u}$
θ_q
q

Figure 14

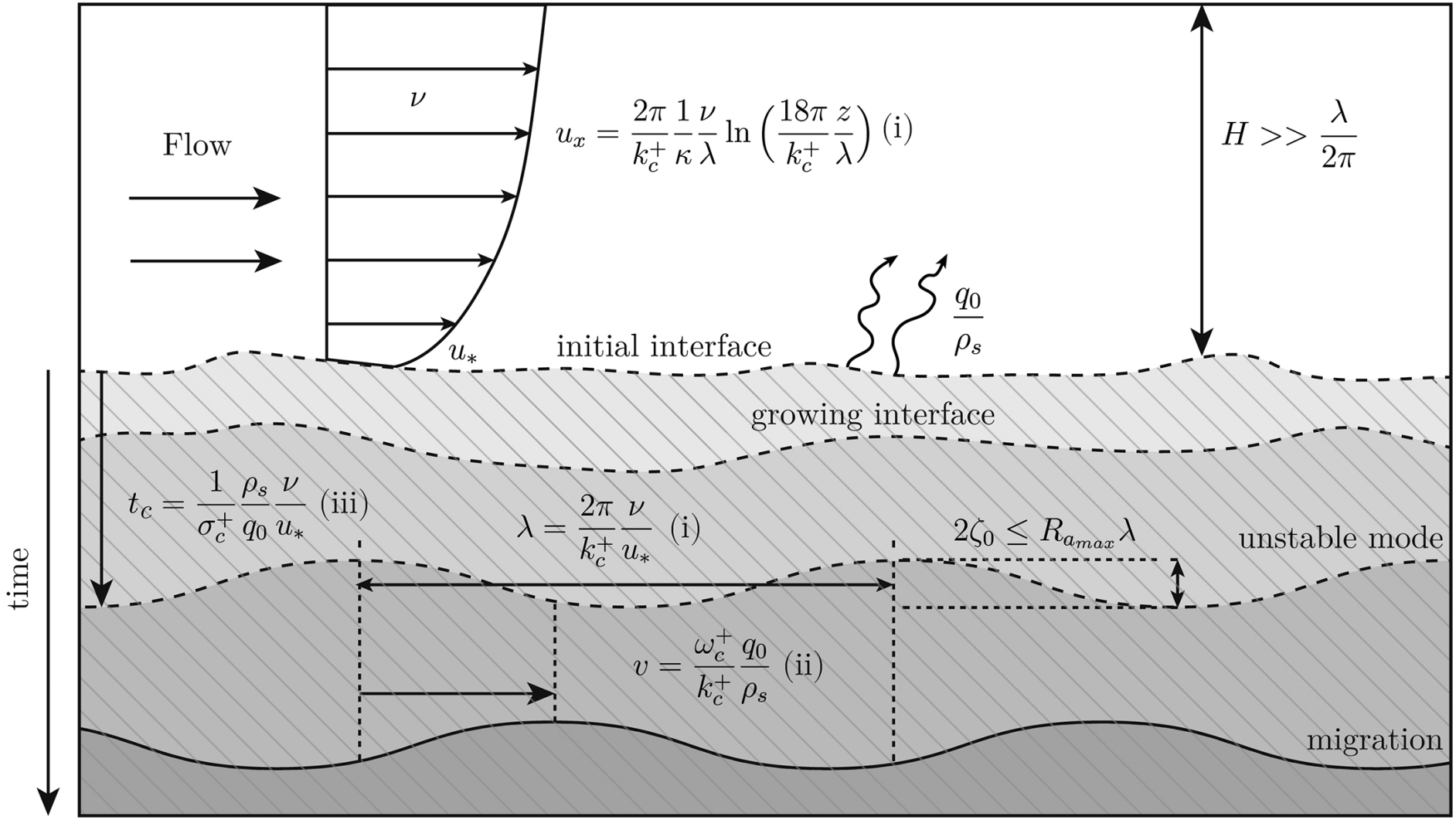
Flow
ν
$u_x = \frac{2\pi}{k_c^+}\frac{1}{\kappa}\frac{\nu}{\lambda}\ln\left(\frac{18\pi}{k_c^+}\frac{z}{\lambda}\right)$ (i)
$H >> \frac{\lambda}{2\pi}$
u_*
initial interface
$\frac{q_0}{\rho_s}$
growing interface
$t_c = \frac{1}{\sigma_c^+}\frac{\rho_s}{q_0}\frac{\nu}{u_*}$ (iii)
$\lambda = \frac{2\pi}{k_c^+}\frac{\nu}{u_*}$ (i)
$2\zeta_0 \leq R_{a_{max}}\lambda$
unstable mode
time
$v = \frac{\omega_c^+}{k_c^+}\frac{q_0}{\rho_s}$ (ii)
migration

Figure 15